Title

Four distinct trajectories of tau deposition identified in Alzheimer's disease

Journal

Nature Medicine, 27(5)

ISSN

1078-8956

Authors

Vogel, Jacob W

Young, Alexandra L

Oxtoby, Neil P

et al.

Publication Date

2021-05-01

DOI

10.1038/s41591-021-01309-6

Peer reviewed

HHS Public Access

Author manuscript

Nat Med. Author manuscript; available in PMC 2021 December 20.

Published in final edited form as:

Nat Med. 2021 May ; 27(5): 871–881. doi:10.1038/s41591-021-01309-6.

*Data used in preparation of this article were obtained from the Alzheimer's Disease Neuroimaging Initiative (ADNI) database (adni.loni.usc.edu). As such, the investigators within the ADNI contributed to the design and implementation of ADNI and/or provided data but did not participate in analysis or writing of this report. A complete listing of ADNI investigators can be found at: :https://adni.loni.usc.edu/wp-content/uploads/how_to_apply/ADNI_Acknowledgement_List.pdf

Correspondence: jacob.vogel@mail.mcgill.ca; oskar.hansson@med.lu.se.

Author Contributions

JWV, OH & ACE conceptualized the work. JWV, ALY, NPO, LMA, MJP & OH contributed to analytic design. MJP, MDD, GDR, CHL & OH acquired and provided the data. RS, RO, OTS & RLJ contributed to data curation and processing. JWV analyzed the data. ALY & DCA originally created the SuStaIn algorithm, and NPO & LMA contributed to its execution. YIM created the ESM algorithm. JWV & OH drafted the manuscript. All authors interpreted the data and substantively contributed to revising the manuscript.

Code Availability statement

Python and MatLab implementations of the SuStaIn algorithm are available on the UCL-POND github page: https://github.com/ucl-pond. The ESM algorithm is available for academics as part of an open-access, user-friendly software (for further details, visit https://www.neuropm-lab.com/).

Alzheimer's Disease Neuroimaging Initiative

Michael Weiner[17], Paul Aisen[18], Ronald Petersen[19], Clifford R. Jack Jr.[19], William Jagust[20], John Q. Trojanowki[21], Arthur W. Toga[22], Laurel Beckett[23], Robert C. Green[24], Andrew J. Saykin[25], John Morris[26], Leslie M. Shaw[27], Enchi Liu[28], Tom Montine[29], Ronald G. Thomas[18], Michael Donohue[18], Sarah Walter[18], Devon Gessert[18], Tamie Sather[18], Gus Jiminez[18], Danielle Harvey[23], Matthew Bernstein[19], Nick Fox[30], Paul Thompson[31], Norbert Schuff[32], Charles DeCArli[23], Bret Borowski[19], Jeff Gunter[19], Matt Senjem[19], Prashanthi Vemuri[19], David Jones[19], Kejal Kantarci[19], Chad Ward[19], Robert A. Koeppe[33], Norm Foster[34], Eric M. Reiman[35], Kewei Chen[35], Chet Mathis[36], Susan Landau[20], Nigel J. Cairns[26], Erin Householder[26], Lisa Taylor Reinwald[26], Virginia Lee[37], Magdalena Korecka[37], Michal Figurski[37], Karen Crawford[22], Scott Neu[22], Tatiana M. Foroud[25], Steven Potkin[38], Li Shen[25], Faber Kelley[25], Sungeun Kim[25], Kwangsik Nho[25], Zaven Kachaturian[39], Richard Frank[40], Peter J. Snyder[41], Susan Molchan[42], Jeffrey Kaye[43], Joseph Quinn[43], Betty Lind[43], Raina Carter[43], Sara Dolen[43], Lon S. Schneider[44], Sonia Pawluczyk[44], Mauricio Beccera[44], Liberty Teodoro[44], Bryan M. Spann[44], James Brewer[45], Helen Vanderswag[45], Adam Fleisher[35], Judith L. Heidebrink[33], Joanne L. Lord[33], Sara S. Mason[19], Colleen S. Albers[19], David Knopman[19], Kris Johnson[19], Rachelle S. Doody[46], Javier Villanueva Meyer[46], Munir Chowdhury[46], Susan Rountree[46], Mimi Dang[46], Yaakov Stern[47], Lawrence S. Honig[47], Karen L. Bell[47], Beau Ances[48], John C. Morris[48], Maria Carroll[48], Sue Leon[48], Mark A. Mintun[48], Stacy Schneider[48], Angela OliverNG[49], Randall Griffith[49], David Clark[49], David Geldmacher[49], John Brockington[49], Erik Roberson[49], Hillel Grossman[50], Effie Mitsis[50], Leyla deToledo-Morrell[51], Raj C. Shah[51], Ranjan Duara[52], Daniel Varon[52], Maria T. Greig[52], Peggy Roberts[52], Marilyn Albert[53], Chiadi Onyike[53], Daniel D'Agostino II[53], Stephanie Kielb[53], James E. Galvin[54], Dana M. Pogorelec[54], Brittany Cerbone[54], Christina A. Michel[54], Henry Rusinek[54], Mony J de Leon[54], Lidia Glodzik[54], Susan De Santi[54], P. Murali Doraiswamy[55], Jeffrey R. Petrella[55], Terence Z. Wong[55], Steven E. Arnold[27], Jason H. Karlawish[27], David Wolk[27], Charles D. Smith[56], Greg Jicha[56], Peter Hardy[56], Partha Sinha[56], Elizabeth Oates[56], Gary Conrad[56], Oscar L. Lopez[36], MaryAnn Oakley[36], Donna M. Simpson[36], Anton P. Porsteinsson[57], Bonnie S. Goldstein[57], Kim Martin[57], Kelly M. Makino[57], M. Saleem Ismail[57], Connie Brand[57], Ruth A. Mulnard[58], Gaby Thai[58], Catherine Mc Adams Ortiz[58], Kyle Womack[59], Dana Mathews[59], Mary Quiceno[59], Ramon Diaz Arrastia[59], Richard King[59], Myron Weiner[59], Kristen Martin Cook[59], Michael DeVous[59], Allan I. Levey[60], James J. Lah[60], Janet S. Cellar[60], Jeffrey M. Burns[61], Heather S. Anderson[61], Russell H. Swerdlow[61], Liana Apostolova[62], Kathleen Tingus[62], Ellen Woo[62], Daniel H. S. Silverman[62], Po H. Lu[62], George Bartzokis[62], Neill R Graff Radford[63], Francine ParfittH[63], Tracy Kendall[63], Heather Johnson[63], Martin R. Farlow[25], Ann Marie Hake[25], Brandy R. Matthews[25], Scott Herring[25], Cynthia Hunt[25], Christopher H. van Dyck[64], Richard E. Carson[64], Martha G. MacAvoy[64], Howard Chertkow[65], Howard Bergman[65], Chris Hosein[65], Sandra Black[66], Bojana Stefanovic[66], Curtis Caldwell[66], Ging Yuek Robin Hsiung[67], Howard Feldman[67], Benita Mudge[67], Michele Assaly Past[67], Andrew Kertesz[68], John Rogers[68], Dick Trost[68], Charles Bernick[69], Donna Munic[69], Diana Kerwin[70], Marek Marsel Mesulam[70], Kristine Lipowski[70], Chuang Kuo Wu[70], Nancy Johnson[70], Carl Sadowsky[71], Walter Martinez[71], Teresa Villena[71], Raymond Scott Turner[72], Kathleen Johnson[72], Brigid Reynolds[72], Reisa A. Sperling[73], Keith A. Johnson[73], Gad Marshall[73], Meghan Frey[73], Jerome Yesavage[74], Joy L. Taylor[74], Barton Lane[74], Allyson Rosen[74], Jared Tinklenberg[74], Marwan N. Sabbagh[75], Christine M. Belden[75], Sandra A. Jacobson[75], Sherye A. Sirrel[75], Neil Kowall[76], Ronald Killiany[76], Andrew E. Budson[76], Alexander Norbash[76], Patricia Lynn Johnson[76], Thomas O. Obisesan[77], Saba Wolday[77], Joanne Allard[77], Alan Lerner[78], Paula Ogrocki[78], Leon Hudson[78], Evan Fletcher[79], Owen Carmichael[79], John Olichney[79], Charles DeCarli[79], Smita Kittur[80], Michael Borrie[81], T Y Lee[81], Rob Bartha[81], Sterling Johnson[82], Sanjay Asthana[82], Cynthia M. Carlsson[82], Steven G. Potkin[83], Adrian Preda[83], Dana Nguyen[83], Pierre Tariot[35], Stephanie Reeder[35], Vernice Bates[84], Horacio Capote[84], Michelle Rainka[84], Douglas W. Scharre[85], Maria Kataki[85], Anahita Adeli[85], Earl A. Zimmerman[86], Dzintra Celmins[86], Alice D. Brown[86], Godfrey D. Pearlson[87], Karen Blank[87], Karen Anderson[87], Robert B. Santulli[88], Tamar J. Kitzmiller[88], Eben S. Schwartz[88], Kaycee M. SinkS[89], Jeff D. Williamson[89], Pradeep Garg[89], Franklin Watkins[89], Brian R. Ott[90], Henry Querfurth[90], Geoffrey Tremont[90], Stephen Salloway[91], Paul Malloy[91], Stephen Correia[91], Howard J. Rosen[17], Bruce L. Miller[17], Jacobo Mintzer[92], Kenneth Spicer[92], David Bachman[92], Elizabether Finger[93], Stephen Pasternak[93], Irina Rachinsky[93], Dick Drost[93], Nunzio Pomara[94], Raymundo Hernando[94], Antero Sarrael[94], Susan K. Schultz[95], Laura L. Boles Ponto[95], Hyungsub Shim[95], Karen Elizabeth Smith[95], Norman Relkin[96], Gloria Chaing[96], Lisa Raudin[96], Amanda Smith[97], Kristin Fargher[97], Balebail Ashok Raj[97]

[17] UC San Francisco, San Francisco, CA, USA

[18] UC San Diego, San Diego, CA, USA

Four distinct trajectories of tau deposition identified in

[19] Mayo Clinic, Rochester, NY, USA
[20] UCL Dementia Centre, UK
[21] U Pennsylvania, Pennsylvania, CA, USA
[22] USC, Los Angeles, CA, USA
[23] UC Davis, Davis, CA, USA
[24] Brigham and Women's Hospital, Harvard Medical School, Boston, MA, USA
[25] Indiana University, Bloomington, IND, USA
[26] Washington University St. Louis, St. Louis, MO, USA
[27] University of Pennsylvania, Philadelphia, PA, USA
[28] Janssen Alzheimer Immunotherapy, South San Francisco, CA, USA
[29] University of Washington, Seattle, WA, USA
[30] University of London, London, UK
[31] USC School of Medicine, Los Angeles, CA, USA
[32] UCSF MRI, San Francisco, CA, USA
[33] University of Michigan, Ann Arbor, MI, USA
[34] University of Utah, Salt Lake City, UT, USA
[35] Banner Alzheimer's Institute, Phoenix, AZ, USA
[36] University of Pittsburgh, Pittsburgh, PA, USA
[37] UPenn School of Medicine, Philadelphia, PA, USA
[38] UC Irvine, Newport Beach, CA, USA
[39] Khachaturian, Radebaugh & Associates, Inc and Alzheimer's Association's Ronald and Nancy Reagan's Research Institute, Chicago, IL, USA
[40] General Electric, Boston, MA, USA
[41] Brown University, Providence, RI, USA
[42] National Institute on Aging/National Institutes of Health, Bethesda, MD, USA
[43] Oregon Health and Science University, Portland, OR, USA
[44] University of Southern California, Los Angeles, CA, USA
[45] University of California San Diego, San Diego, CA, USA
[46] Baylor College of Medicine, Houston, TX, USA
[47] Columbia University Medical Center, New York, NY, USA
[48] Washington University, St. Louis, MO, USA
[49] University of Alabama Birmingham, Birmingham, MO, USA
[50] Mount Sinai School of Medicine, New York, NY, USA
[51] Rush University Medical Center, Chicago, IL, USA
[52] Wien Center, Vienna, Austria
[53] Johns Hopkins University, Baltimore, MD, USA
[54] New York University, New York, NY, USA
[55] Duke University Medical Center, Durham, NC, USA
[56] University of Kentucky, city of Lexington, NC, USA
[57] University of Rochester Medical Center, Rochester, NY, USA
[58] University of California, Irvine, CA, USA
[59] University of Texas Southwestern Medical School, Dallas, TX, USA
[60] Emory University, Atlanta, GA, USA
[61] University of Kansas, Medical Center, Lawrence, KS, USA
[62] University of California, Los Angeles, CA, USA
[63] Mayo Clinic, Jacksonville, FL, USA
[64] Yale University School of Medicine, New Haven, CT, USA
[65] McGill Univ., Montreal Jewish General Hospital, Montreal, WI, USA
[66] Sunnybrook Health Sciences, Toronto, ON, Canada
[67] U.B.C. Clinic for AD & Related Disorders, British Columbia, BC, Canada
[68] Cognitive Neurology St. Joseph's, Toronto, ON, Canada
[69] Cleveland Clinic Lou Ruvo Center for Brain Health, Las Vegas, NV, USA
[70] Northwestern University, Evanston, IL, USA
[71] Premiere Research Inst Palm Beach Neurology, West Palm Beach, FL, USA
[72] Georgetown University Medical Center, Washington, DC, USA
[73] Brigham and Women's Hospital, Boston, MA, USA
[74] Stanford University, Santa Clara County, CA, USA
[75] Banner Sun Health Research Institute, Sun City, AZ, USA
[76] Boston University, Boston, MA, USA
[77] Howard University, Washington, DC, USA
[78] Case Western Reserve University, Cleveland, OH, USA
[79] University of California, Davis Sacramento, CA, USA
[80] Neurological Care of CNY, New York, NY, USA
[81] Parkwood Hospital, Parkwood, CA, USA

Alzheimer's disease

Jacob W. Vogel[1], **Alexandra L. Young**[2], **Neil P. Oxtoby**[3,4], **Ruben Smith**[5,6], **Rik Ossenkoppele**[5,7], **Olof T. Strandberg**[5], **Renaud La Joie**[8], **Leon M. Aksman**[3,9], **Michel J Grothe**[10,11], **Yasser Iturria-Medina**[1], **Alzheimer's Disease Neuroimaging Initiative***, **Michael J. Pontecorvo**[12], **Michael D. Devous**[12], **Gil D. Rabinovici**[8,13], **Daniel C. Alexander**[3,4], **Chul Hyoung Lyoo**[14], **Alan C. Evans**[1], **Oskar Hansson**[5,15]

[1]Montreal Neurological Institute, McGill University, Montréal, QC, Canada

[2]Department of Neuroimaging, Institute of Psychiatry, Psychology and Neuroscience, King's College London, London, UK.

[3]Centre for Medical Image Computing, University College London, London, WC1E 6BT, UK

[4]Department of Computer Science, University College London, London, WC1E 6BT, UK

[5]Clinical Memory Research Unit, Lund University, Lund, Sweden

[6]Department of Neurology, Skåne University Hospital, Lund, Sweden

[7]Alzheimer Center Amsterdam, Department of Neurology, Amsterdam Neuroscience, Vrije Universiteit Amsterdam, Amsterdam UMC, Amsterdam, The Netherlands

[8]Memory and Aging Center, Department of Neurology, Weill Institute for Neurosciences, University of California, San Francisco, San Francisco, CA

[9]Department of Medical Physics and Biomedical Engineering, University College London, London, WC1E 6BT, UK

[10]Wallenberg Centre for Molecular and Translational Medicine, University of Gothenburg, Gothenburg, Sweden

[11]Instituto de Biomedicina de Sevilla, Hospital Universitario Virgen del Rocío/CSIC/Universidad de Sevilla, Seville, Spain

[12]Avid Radiopharmaceuticals, Philadelphia, PA, USA

---

[82] University of Wisconsin, Madison, WI, USA
[83] University of California, Irvine BIC, Irvine, CA, USA
[84] Dent Neurologic Institute, Amherst, MA, USA
[85] Ohio State University, Columbus, OH, USA
[86] Albany Medical College, Albany, NY, USA
[87] Hartford Hosp, Olin Neuropsychiatry Research Center, Hartford, CT, USA
[88] Dartmouth Hitchcock Medical Center, Albany, NY, USA
[89] Wake Forest University Health Sciences, Winston-Salem, NC, USA
[90] Rhode Island Hospital, Rhode Island, USA
[91] Butler Hospital, Providence, RI, USA
[92] Medical University South Carolina, Charleston, SC, USA
[93] St. Joseph's Health Care, Toronto, Canada
[94] Nathan Kline Institute, Orangeburg, SC, USA
[95] University of Iowa College of Medicine, Iowa City, IA, USA
[96] Cornell University, Ithaca, NY, USA
[97] University of South Florida: USF Health Byrd Alzheimer's Institute, Tampa, FL 33613 USA

[13]Department of Radiology and Biomedical Imaging; University of California, San Francisco, San Francisco, CA

[14]Departments of Neurology, Gangnam Severance Hospital, Yonsei University College of Medicine, Seoul, Republic of Korea

[15]Memory Clinic, Skåne University Hospital, Malmö, Sweden

Abstract

Alzheimer's disease (AD) is characterized by spread of tau pathology throughout the cerebral cortex. The spreading pattern was thought to be fairly consistent across individuals, though recent work has demonstrated substantial variability in the AD population. Using tau-PET scans from 1612 individuals, we identified four distinct spatiotemporal trajectories of tau pathology, ranging in prevalence from 18 to 33%. We replicated previously described limbic-predominant and medial temporal lobe-sparing patterns, while also discovering posterior and lateral temporal patterns resembling atypical clinical variants of AD. These "subtypes" were stable during longitudinal follow-up, and were replicated in a separate sample using a different radiotracer. The subtypes presented with distinct demographic and cognitive profiles, and differing longitudinal outcomes. Additionally, network diffusion models implicated that pathology originates and spreads through distinct corticolimbic networks in the different subtypes. Together, our results suggest variation in tau pathology is common and systematic, perhaps warranting a re-examination of the notion of "typical AD", and a revisiting of tau pathological staging.

Introduction

Alzheimer's disease (AD) is the leading cause of dementia worldwide and prevalence is expected to double in the next twenty years[1]. At autopsy, AD presents with diffuse extracellular and neuritic amyloid-β (Aβ) plaques, and intracellular neurofibrillary tangles and neuropil threads of hyperphosphorylated tau, along with extensive neurodegeneration[2,3]. Leading hypotheses have postulated these two hallmark proteins, Aβ and tau, either alone or in combination, are causative agents in disease etiology and progression[4,5]. Cortical tau colocalizes with cortical atrophy and predicts future neurodegeneration[6], while the appearance of tau in specific cognitive networks leads to domain-specific cognitive impairments[7]. Recently, the focus of treatment discovery has shifted to tau, and numerous therapeutic interventions are currently undergoing research and development. A better understanding of tau pathophysiology is therefore of imminent need in order to aid development of these interventions.

Tau tangles are thought to exhibit a stereotypical pattern of cortical spread, which has been formalized into the Braak staging system[8,9]. The six Braak stages describe the first appearance of cortical tau tangles in the transentorhinal cortex, subsequent spread throughout the medial and basal temporal lobes, then into neocortical associative regions, and finally into the unimodal sensory and motor cortex[9]. While this stereotyped progression was derived from histopathological staining at autopsy, tau can now be measured *in vivo* in the human brain using positron emission tomography (PET). Early tau-PET imaging

studies described average spatial patterns that have mostly converged with the Braak staging system[10,11].

However, many examples have emerged of individual tau patterns that do not fit neatly into the Braak staging system. A medial temporal lobe (MTL)-sparing phenotype with extensive cortical tau burden but limited MTL burden has been described, as well as a limbic-predominant phenotype with most prominent tau pathology in limbic and medial temporal cortex, which were found to be associated with specific patient profiles[12–14]. In addition, clinical variants of AD have been described that exhibit specific patterns of pathology that deviate from the Braak staging scheme[15], e.g., posterior cortical atrophy (PCA) [16], logopenic primary progressive aphasia (lvPPA)[17], and others[18]. These latter clinical variants of AD are relatively uncommon and most frequently associated with early-onset AD, but represent another example of atypical tau patterning.

Taken together, the examples above suggest that, while the Braak staging system appears to be a good description of tau spreading at the population level, it does not account for systematic variability at the individual level. Variation in tau patterning may be indicative of distinct underlying neurobiology [19,20], which may affect treatment response. Different subtypes may also have distinct rates and profiles of cognitive decline [21,22], potentially affecting clinical trials. For these reasons, a systematic description of variation in AD pathological spread is needed. Previous studies have provided invaluable information toward this effort [12,13,23–26], but carry certain limitations. Pathology studies, for example, are limited by spatial sampling and semi-quantitation. Neuroimaging studies overcome some of those limitations, but often use non-specific measurements, and rely on methods designed to parse spatial rather than spatiotemporal variation.

Here we present a systematic characterization of heterogeneity in tau patterning in AD. We amassed the largest and most diverse sample of tau-PET data to date (n=2324), covering the full clinical spectrum from asymptomatic through mild cognitive impairment (MCI) to AD dementia, allowing unprecedented power to detect and characterize AD subtypes. We fit this data using the Subtype and Stage Inference (SuStaIn) model, a paradigm-shifting algorithm that combines disease progression modeling with traditional clustering to achieve probabilistic spatiotemporal partitioning and classification[23]. SuStaIn requires only cross-sectional datasets to automatically detect multiple spatiotemporal trajectories, and it provides probabilistic and quantitative information for individualized inference. We apply SuStaIn to our multi-cohort sample of tau-PET data to discover systematic spatiotemporal variation in tau spreading. We validate the subtypes across different PET radiotracers, and we validate the progression patterns using serial longitudinal tau-PET data.

Results

We compiled an initial sample of 1667 individuals with flortaucipir-PET tau images, spanning five separate cohorts. 1143 individuals were identified as either cognitively normal (n=707), or showed biomarker evidence for Aβ pathology (Aβ+ MCI, n=223; Aβ+ AD dementia, n=213), and were used as a discovery sample for subsequent analysis. Demographic information and cross-cohort comparisons can be found in Table S1.

Spatiotemporal subtypes of Alzheimer's disease.

We applied the SuStaIn algorithm (Extended Data Fig. S1a) to the 1143 flortaucipir-PET images in order to extract distinct spatiotemporal trajectories of tau spreading. As expected, many individuals (n=700; 61%) did not demonstrate any abnormal tau-PET signal, and were therefore automatically assigned to a tau-negative group (S0) (see Supplementary Note 1). Using cross-validation, we determined a four-subtype solution to best represent the remaining data (n=443; See Methods, Extended Data Fig. S1c–f). The four-subtype model was applied to probabilistically assign individuals to one of 30 progressive stages along one of the four subtype trajectories (Fig 1).

The distribution of clinical diagnoses across stages and subtypes can be found in Extended Data Fig. S2f,g,i. 145 (32.7%) individuals exhibited a limbic-predominant phenotype, with a Braak-like spatial progression across SuStaIn stages (S1: Limbic). An additional 79 individuals (17.8%) expressed a parietal-dominant and MTL-sparing phenotype, where early precuneus binding accumulated across temporoparietal and frontal cortex, but with relative sparing of the MTL (S2: MTL-Sparing). The third subtype composed 135 (30.5%) individuals with a predominant posterior occipitotemporal phenotype, involving early occipital lobe binding and gradual anterior progression across SuStaIn stage (S3: Posterior). The remaining 84 (19.0%) individuals showed a temporoparietal phenotype with distinct left-sided lateralization, characterized by early left-temporal tau eventually spreading to parietal and frontal cortex across disease stage (S4: Lateral [L] Temporal). The differences highlight inconsistencies between tau-PET binding and pathological sequencing of specific brain regions found in previous studies, such as the hippocampus, lingual gyrus and insula[10,11,27], which exhibited different binding patterns across subtypes (Extended Data Fig. S3).

Stability of AD subtypes.

While variation in subtype proportion was observed (and expected) across cohorts, all subtypes were represented across all cohorts (Extended Data Fig. S4). Most individuals fell neatly into the stereotypical progression of each subtype (Fig 1b), allowing a clean stepwise progression across tau abnormality events to be observed across each subtype population (Extended Data Fig. S5). 12% of individuals did not fall cleanly into any subtype due to having either too little or too much pathology, both of which are uninformative for subtype (Fig 1b, Extended Data Fig. S2d,h). In general, early stage and cognitively normal individuals were assigned to subtypes with less confidence, though median subtype probability neared 100% by SuStaIn stage 7 (Extended Data Fig. S2e), and by the MCI clinical stage (Extended Data Fig. S2h). This provides evidence that the earliest phases of each subtype may overlap, or that they are difficult to distinguish above measurement error. We further confirmed that the subtypes produced by SuStaIn were not driven by, or specific to, arbitrary user inputs relating to the anchoring of regional pseudotimes (Methods, Extended Data Fig. S6).

We next assessed whether the same subtypes could be derived within a separate replication sample of 469 individuals scanned with the RO948 tau-PET tracer. The replication cohort, BioFINDER II[28], is described in Supplementary Table S1. SuStaIn was run separately

on these individuals, constraining the analysis to produce four subtypes. Three of the four replication subtypes greatly resembled those derived in the discovery sample (Fig 2). The only exception involved the S4: L Temporal subtype, which had a similar overall tau-PET pattern but involved right-sided rather than left-sided lateralization. Further analysis determined that this related to the smaller sample size rather than the differing radiotracer, and further suggested that the S4: L Temporal subtype has a consistent overall pattern but a high propensity for marked lateralization (see Supplemental Note 2, Extended Data Fig. S7).

Subtypes characterized by distinct clinical profiles.

Next, we compared demographic, cognitive and genetic (i.e. APOE4 status) variables between the subtypes and the tau-negative S0 group (Table 1). Individuals across all four subtypes expressed worse MMSE and worse memory scores compared to S0 individuals. In addition, all subtypes except S1 (Limbic) had worse global cognitive composite scores, individuals across all subtypes except S2 (MTL-Sparing) were more likely to be *APOE4* carriers, and all subtypes except S4 (L Temporal) were more likely to be female, compared to S0 individuals. Compared to tau-negative individuals in S0, S1 and S3 were older, S2 exhibited poorer executive function, S2 and S3 exhibited poorer visuospatial function, and S4 had worse language scores.

Compared to other subtypes (i.e., other tau-positive individuals), individuals within the S1 (Limbic) subtype were more likely to be *APOE4* carriers, had less overall tau with a more right-sided pattern, and had better overall cognition, but worse memory relative to their overall cognition. S2 (MTL Sparing) individuals were younger, less likely to carry an *APOE4* allele, had more overall tau burden, had a more right-sided tau pattern and had worse relative executive function, compared to other subtypes. S4 (L Temporal) individuals had more overall tau with a more left-lateralized pattern. These individuals also trended at having worse overall cognition, but had better relative memory and worse relative language scores compared to other subtypes. Finally, individuals with the S3 (Posterior) subtype did not exhibit any significant cognitive, demographic or *APOE4* differences compared to the other subtypes. These relationships (after adjustment for demographics, diagnosis, cohort and SuStaIn stage) are described in Table 1 and visualized in Extended Data Fig. S8.

Each individual was assigned a stage along their respective subtype trajectory. As expected, increasing SuStaIn stage was associated with worse global cognition as measured with MMSE ($r=0.54$, $p<0.0001$; Fig 3a). This relationship was consistent across all subtypes (S1: $r = -0.51$, S2: $r = -0.53$, S3: $r = -0.64$, S4: $r = -0.40$, all $p<0.001$). A strong negative relationship between SuStaIn stage and age was also observed, such that individuals at later SuStaIn stages tended to be younger ($r = -0.59$, $p<0.0001$). This relationship was again consistent across all subtypes, though less prominent for S1 (S1: $r = 0.20$, S2: $r = -0.68$, S3: $r = -0.64$, S4: $r = -0.73$, all $p<0.05$; Fig 3b). This inverse relationship was also present among individuals both 65 and younger ($n = 100$, $r = -0.43$, $p <0.0001$) and individuals older than 65 ($n = 342$, $r = -0.28$, $p < 0.0001$), suggesting the effect is not driven purely by early onset cases. Lateralization also increased with increasing SuStaIn stage (Extended Data Fig. S9). However, despite trends in lateralization at higher SuStaIn stage, many individuals were observed with a “reversed” lateralization compared to the group average

tau lateralization patterns for their subtype (Extended Data Fig. S9), suggesting lateralization to be at least partially orthogonal with subtype.

Cognitive prognosis of AD subtypes.

Longitudinal MMSE data was available for a subset of 697 individuals (mean follow-up = 1.74 years from PET scan, sd = 0.64). Individuals with the S3 (Posterior) subtype had significantly slower decline compared to all other subtypes independently (S1: t=2.03, p=0.043; S2: t=2.88, p=0.004; S4: t=4.83, p<0.0001), as well as in a one vs all analysis (t=3.64,p=0.0003; Fig 3c). This finding persisted across different clinical diagnoses (Fig 3d, Supplemental Table S2), and was confirmed through a meta-analysis across the five cohorts, which also showed a significantly slower decline for the S3 (Posterior) group (t=1.67,p=0.047; Fig 3e). Individuals with the S4 (L Temporal) subtype additionally showed steeper cognitive decline compared to S1 (Limbic) subtype individuals (t=3.40, p=0.0008), and generally showed faster decline compared to other subtypes in a one vs all analysis (t=−4.49,p<0.0001) and across clinical diagnoses (Fig 3d, Supplementary Table S2). A meta-analysis once again confirmed a significant overall effect (t=1.88,p=0.031; Fig 3e).

Stability and progression of AD subtypes over time.

SuStaIn uses cross-sectional data to infer longitudinal trajectories for the tau data, so evaluating how well longitudinal data fits the model is a key aspect of validation. 519 individuals from the discovery sample also had follow-up flortaucipir-PET scans (mean follow-up time = 1.42, sd = 0.58, years). Overall, 88.5% of individuals exhibited the same subtype at both baseline and follow-up, or progressed from S0 into a subtype (Fig 3f). Stability when excluding individuals classified as S0 at baseline (tau-positive stability) and follow-up was 83.9%. Stable individuals were classified with a higher degree of confidence at baseline compared to individuals whose subtype changed at follow-up (stable mean = 0.91, sd = 0.17; change mean = 0.74, sd = 0.27; t = 5.26, p < 0.0001; Fig 3g). Supplementary Table S3 shows longitudinal tau-positive stability (i.e. excluding S0) when excluding individuals using various subtype probability thresholds.

We next examined how SuStaIn stage changed over time for each subtype. Across the whole sample, we observed significant yearly increase in SuStaIn stage (mean Δ/year = 0.8, t[148]=6.54, p<0.0001) (Fig 3h, Table S4), and a significant difference in mean annual rate of SuStaIn stage change was seen across subtypes (details in Supplementary Note 3). The annual SuStaIn stage increased faster in S4 (L Temporal) compared to S2 (MTL-Sparing) and S3 (Posterior) subtypes (Fig 3h, Supplementary Note 3). Younger age (r=−0.22, p=0.006), but not higher baseline SuStaIn stage (r = 0.12, p=0.15), was associated with faster annual change in stage. As a final validation, we used SuStaIn to forecast longitudinal rate of regional tau-PET change at the individual level. On average, predictions were significantly better than chance for all subtypes (S1 (Limbic): t[78]=5.00, p<0.0001; S2 (MTL-Sparing): t[52]=2.16, p=0.035; S3 (Posterior): t[45]=3.05, p=0.0039; S4 (L Temporal): t[29]=4.93, p<0.0001; Fig 3i).

Subtype patterns resemble distinct cortico-limbic networks.

Based on our previous work[29], we used network diffusion models to examine the possibility that the observed subtype-specific tau spreading patterns may be driven by spread through distinct networks. We found that an entorhinal cortex epicenter was optimal for the S1 (Limbic) subtype tau pattern and strongly replicated the pattern of tau spreading (r^2=0.70), but did not reproduce other subtype patterns nearly as well (S2: r^2=0.04; S3: r^2=0.41; S4: r^2=0.37). Models using different epicenters substantially improved fit for these others subtypes (Fig 4a,b,e): best fitting models used the middle temporal gyrus (r^2=0.27) for S2 (MTL-Sparing), the fusiform gyrus (r^2=0.59) for S3 (Posterior) and the inferior temporal gyrus (r^2=0.50) for S4 (L Temporal) (Fig 4c), suggesting a possible predominance of these regions in secondary tau seeding for different subtypes. Highly similar results were found using a different brain atlas and different connectivity data (Extended Data Fig. S10). We further tracked how the best-fitting epicenter changed at higher disease stages, perhaps reflecting participation of different regions as secondary seeding points with advancing disease progression (Fig 4d). All but the S2 (MTL-Sparing)_subtype exhibited MTL spreading in earlier stages, whereas early stages of S2 involved parietal spread. Later stages involved secondary seeding in the temporal lobes, as well as subtype-specific regions. Together, these results suggest that distinct tau patterns across different subtypes may be driven in part by vulnerability of, or selective spread through, distinct temporal lobe networks.

Discussion

For the last thirty years, the progression of tau pathology in AD has principally been described by a single model of spatiotemporal evolution[8,9], despite frequent examples of nonconforming cases[12]. We show that the cortical cascade of tau pathology is better described by a data-driven model including multiple spatiotemporal patterns (Fig. 5). Importantly, our findings may reconcile atypical AD variants with common variations of typical AD into a single unified model of pathological progression. First, the model reaffirms the existence of observed cortical-predominant and limbic-predominant pathological patterns as distinct subtypes of tau progression, rather than phases along a continuum. In addition, the model also accounts for the most frequently occurring atypical clinical variants of AD, PCA and lvPPA, as the extremes of regularly occurring posterior and lateral-temporal AD subtypes. Together, our data align with a recent model[14] to suggest variation in the pathological expression of AD along two orthogonal axes: subtype and severity, the latter of which is strongly and inversely correlated with age (Fig 5). Given that no dominant pattern emerged, our data suggest the existence of multiple common AD subtypes, challenging the notion that there is such a pathological entity that can be described as “typical” AD. Rather, the spatial pattern of tau spreading appears to vary along at least four archetypes, depending on factors such as age and genotype. Therefore, we propose heterogeneity in AD is best represented as a quadrilateral axis (Fig 5).

Our results are robust across datasets and radiotracers. We found individuals representing each of four subtype patterns in each of the five contributing cohorts, and we reproduced a very similar set of subtypes in a totally separate sample using a different radiotracer.

Further, most individuals were confidently assigned into one subtype pattern, which was consistent over time. The limbic subtype was the most frequent, and presented with many characteristics typically associated with AD, including a greater proportion of *APOE4* carriers, a strongly amnestic phenotype, and medial temporal pathology with a Braak-like progression of tau spread. However, this subtype represented only a third of all tau-positive cases in our dataset (though the earliest stages of three of the four subtypes featured prominent MTL binding, Fig 4d). Our data suggest instead that, at older onset ages or earlier disease stages, the subtypes may present with subtle differences that may be difficult to detect in the clinic, while at younger onset ages or later stages, the more aggressive phenotype can amplify the distinct subtype expressions. The existence of these phenotypes, if further validated, may necessitate a reform in pathological tau staging, where key regions are surveyed to increase sensitivity to detect subtype-specific patterns.

Many pioneering studies have noted variation in AD pathology. For example, limbic-predominant and MTL-sparing phenotypes are contrasted against “typical” phenotypes that express tau pathology in both the MTL and neocortex[12,13]. In contrast to this notion, we found a subtype of individuals expressing both cortical and MTL tau exhibiting a more aggressive phenotype with marked lateralization, the latter being a feature that has not been well characterized in histopathological studies of AD, which typically assess only one hemisphere. In addition, our model allows the concurrence of MTL and cortical pathology at later stages of several distinct progressions, perhaps suggesting that solely contrasting cortical and MTL tau (e.g. [21,22]) may not be sufficient to describe AD heterogeneity. Indeed, while some spatial convergence could be observed in our AD subtypes, particularly at early or late stages, subtle regional variation consistently distinguishes individuals of one subtype from another.

We reproduce previous reports describing a strong negative correlation between age and tau progression[30–34], as well as previous reports that a younger age of onset of AD is associated with a more rapid progression of tau pathology[35,36]. Interestingly, in our study, this phenomenon was observable across all subtypes (Fig 3b). Previous work has noted that early-onset AD (EOAD) is more likely to present with an atypical (i.e. nonamnestic) phenotype[37]. This may be a specific characteristic of EOAD. However, ours and others studies[26,38,39] suggest that posterior or left-lateralized temporal binding are not uncommon across the age spectrum, but our data suggest that the phenotype is more pronounced at earlier ages. Therefore, atypical variants of AD may represent an accelerated and intensified manifestation of common AD subtypes, though this will require further validation.

Our findings complement other supervised and unsupervised AD subtyping studies from the imaging and pathology literature[12–14,21,22,26,38], though our analysis also produced some novel findings worth further investigation. Despite the extreme of the posterior subtype being represented by PCA, an aggressive disease variant, the posterior subtype overall demonstrated slower cognitive decline compared to all other subtypes. These individuals exhibited considerable tau pathology in posterior (including occipital) brain regions, but also relatively less MTL and frontal binding. These findings, however, are in agreement with pathology literature describing common variation in occipital tau pathology in both preclinical and symptomatic AD [2,40–42]. These studies, variously surveying Brodmann areas

17, 18 and 19, find evidence for occipital lobe tau in 24–52% of sampled brains, including in cognitively normal individuals. Our study suggests this population variation may indeed be systematic, and could be associated with a specific progression pattern. However, tau in the occipital lobe remains understudied, and future studies will be necessary to validate the precise characteristics of this posterior subtype. It is still unclear if the posterior subtype is related to PCA beyond a shared predominance of posterior tau, though it may at least signify the existence of a posterior cortical network selectively vulnerable to tau pathology.

Different manifestations of AD may represent subtle variations in the spread of pathology, or could signal the influence of highly distinct processes relevant to treatment intervention. For example, a recent pathology study found increased NFT pathology and neuronal loss in the cholinergic basal forebrain specifically in patients with a MTL-sparing phenotype, and that earlier disease onset was associated with more NFT pathology in these subjects[43]. Furthermore, another recent study indicated that a targeted basal forebrain treatment could be most effective for patients with a MTL-sparing phenotype[44]. This research may suggest a unique role of the basal forebrain in certain subtypes of AD. Meanwhile, APOE has been consistently associated with limbic manifestations of AD[12,34], including the present study, and APOE or hippocampus-focused therapies could prove more effective for these individuals. Together, these results point to the possibility that clinical trials may benefit from stratification or enrichment based on AD subtype, or as a first step, post-hoc identification of within-subtype effects.

There are currently very few explanations as to why subtypes of AD manifest. Fascinating work has found PCA and lvPPA patients are more likely to exhibit learning disabilities in childhood[45,46], perhaps mediated by abnormalities during brain development[47]. While lvPPA and PCA may represent extremes along the AD continua (as indicated by the present results), this points to the possibility that distinct subtypes may be influenced by variation in cognitive development or other premorbid factors. Another possible explanation for subtypes is interactions between post-translational tau modification and synaptic tau spreading. Several studies have shown that the regional pattern of pathological tau expression in mice is dependent on conformation and injection site of tau seeds[35,48,49]. It is therefore possible that subtypes of tau spread may simply be dictated by distinct tau conformations and/or systematic variation in the human connectome, perhaps at key synaptic junctures. Supporting the latter hypothesis, we found the tau-PET pattern of AD subtypes resembled macroscale neuronal networks seeded from different brain regions. These findings do not presuppose tau pathology necessarily starts in different regions, but instead that different regions may play a more prominent role in tau propagation across subtypes as “amplifying nodes”. This could be mediated by involvement of distinct neuronal cell subtypes[50], which may incur disrupted development due to environmental or genetic factors, leading to network abnormality during life and network vulnerability in late life.

This study has a number of limitations. The SuStaIn method fits data based on the assumption that several discrete sequences are represented within the data, and it uses cross-sectional information to create pseudo-longitudinal sequences. This framework is based off of the same logic as most pathological staging schema (e.g. [8]) and hypotheses of biomarker trajectories (e.g. [5]), but does so in an automated fashion. It is therefore

possible that a SuStaIn subtype trajectory could be created by "appending" or "stitching" unrelated disease states together. However, we did find most individuals to remain the same subtype at longitudinal follow up, and we could predict regional individual tau accumulation greater than chance using just the SuStaIn model. While the use of tau-PET imaging is a great improvement over using MRI to measure AD pathology, there is still some discrepancy between tau-PET signal and true tau pathology[51]. While flortaucipir binds to paired-helical filament tau, off-target binding is an issue with flortaucipir, particularly in the striatum, white matter and choroid plexus[52]. We mitigated this issue by regression of choroid plexus signal, exclusion of subcortical ROIs and non-AD dementia patients, and region-specific normalization against non-specific binding, as well as replication with RO948 which exhibits less off-target binding[53]. Similarly, recent reports question whether elevated flortaucipir binding is detectable before advanced stages of tau accumulation[54–56]. However, SuStaIn's modeling is based on relative regional differences in pathology, and regional variation in tau-PET and tau pathology are correlated[55–57]. Still, while the unbiased spatial sampling of tau-PET data across the brain aided our discovery of these subtype patterns, they must still be validated using histopathology studies. Sample size was an obvious strength of our study, but it comes with the caveat of mixing data from multiple cohorts, scanners, and cognitive batteries. We addressed this issue somewhat by examining subtypes in each cohort separately, replicating our results in a separate sample and adjusting for cohort in our comparisons. In addition, despite our study boasting the largest tau-PET sample to date, even larger samples would be preferable in order to elucidate the spatiotemporal progression of each subtype in more detail. We arrived at a four-subtype solution to describe our data using established statistical methodology to identify a solution the data supports with confidence. However, this does not preclude the possibility that other, more subtly disctinct subtypes exist (Extended Data Fig. S1f).

In conclusion, we describe four distinct but stable spatiotemporal phenotypes of tau accumulation in AD. These subtypes exhibit differing clinical profiles and longitudinal outcomes, and their tau patterns resemble distinct temporal lobe networks. Our data-driven results call into question whether "typical AD" is a quantifiable entity, rather suggesting that several AD subtypes exist, and that their individual differences are exacerbated by more aggressive phenotypes with younger onset ages. Future studies should seek to validate the existence and temporal evolution of these subtypes, as well as identify genetic, cellular and developmental factors that may influence their expression. This may include identifying differences in brain activity and connectivity between individuals, as well as differences in regional vulnerability. This framework may also be useful for enrichment of clinical trials, for providing more individualized clinical care, and eventually for more individualized treatment.

Online Methods

Unless otherwise noted, all data analysis was conducted, and all figures were created, using Python v.3.7.3, mostly using the numpy, scipy, pandas, scikit-learn, nilearn, matplotlib, seaborn and statsmodels libraries.

Sample Characteristics.

The total sample for the following analyses comprised of flortaucipir tau-PET scans from 1667 individuals from five different cohorts (BioFINDER I, Seoul, AVID, UCSF, ADNI), and RO948 PET scans from 657 individuals from a sixth cohort (BioFINDER II). Information pertaining to recruitment, diagnostic criteria and Aβ positivity assessment for the BioFINDER I (BioF)[46], ADNI[27], AVID[32], Seoul[59], UCSF[6] and BioFINDER II (BF2)[28] cohorts have been previously reported. Informed written consent was provided for all participants or their designated caregiver, and all protocols were approved by each cohort's respective institutional ethical review board. Specifically: All BioFINDER subjects provided written informed consent to participate in the study according to the Declaration of Helsinki; ethical approval was given by the Ethics Committee of Lund University, Lund, Sweden, and all methods were carried out in accordance with the approved guidelines. Approval for PET imaging was obtained from the Swedish Medicines and Products Agency and the local Radiation Safety Committee at Skåne University Hospital, Sweden. For UCSF, the study was approved by the University of California (San Francisco and Berkeley) and Lawrence Berkeley National Laboratory institutional review boards for human research. Data from the AVID sample were collected in compliance with the Declaration of Helsinki and the International Conference on Harmonization guideline on good clinical practice. Data collection for the Gangnam Severance hospital sample was approved by the institutional review board of Gangnam Severance Hospital. Information related to participant consent in ADNI can be found at (ADNI; http://adni.loni.usc.edu). Some of the data used in the preparation of this article were obtained from the Alzheimer's Disease Neuroimaging Initiative (ADNI) database (adni.loni.usc.edu). The ADNI was launched in 2003 as a public-private partnership, led by Principal Investigator Michael W. Weiner, MD. The primary goal of ADNI has been to test whether serial magnetic resonance imaging (MRI), positron emission tomography (PET), other biological markers, and clinical and neuropsychological assessment can be combined to measure the progression of mild cognitive impairment (MCI) and early Alzheimer's disease (AD). For up-to-date information, see www.adni-info.org.

From this total sample of 1667 subjects with flortaucipir scans, a subsample was derived including i) all cognitively unimpaired individuals older than 40 years; and ii) individuals who had both a diagnosis of MCI or AD, *and* imaging or fluid evidence of brain Aβ pathology. All subjects with a primary diagnosis other than cognitively unimpaired (which included subjective cognitive decline), MCI or AD were excluded. This subsample, used for all subsequent analysis, comprised 1143 individuals. The same screening procedures were used to filter individuals from BioFINDER II, reducing the samples size from 657 to 469. Characteristics of all samples, including inter-cohort differences, are detailed in Table S1.

Image Acquisition and Preprocessing.

Tau-PET data acquisition procedures for each cohort have been previously described[6,27,28,32,46,59]. All tau-PET data were processed centrally in Lund by analysts blinded to demographic and clinical data, in a manner previously described[46]. Briefly, resampling procedures were used to harmonize image size and voxel dimension across sites. Each image underwent motion correction using AFNI's 3dvolreg (https://

afni.nimh.nih.gov/), and individual PET volumes were averaged within-subject. Each subject's mean PET image next underwent rigid coregistration to it's respective skull-stripped native T1 image, and images were intensity normalized using an inferior cerebellar gray reference region, resulting in standardized update value ratio (SUVR) images. T1 images were processed using Freesurfer v6.0 (https://surfer.nmr.mgh.harvard.edu/), resulting in native space parcellations of each subject's brain using the Desikan-Killiany (freesurfer) atlas. These parcellations were used to extract mean SUVR values within different regions of interest (ROIs) for each subject in native space.

Subtype and Stage Inference.

Typical efforts to perform data-driven subtyping of neuroimages in AD are limited by the confound of disease stage. In a sample spanning the AD spectrum from healthy to demented such as ours, disease progression represents the main source of variation in MR and PET images. Therefore, unless disease stage is somehow accounted for, most clustering algorithms will partition individuals based on their disease stage. This is not useful for parsing heterogeneous patterns related to progression subtypes, which are theoretically orthogonal to disease progression itself. The Subtype and Stage Inference (SuStaIn)[23] algorithm surmounts this limitation by combining clustering with disease progression modeling. Detailed formalization of SuStaIn has been published previously[23].

SuStaIn models linear transition across discrete points along a progression of indices of severity (typically z-scores), separately across different ROIs (Fig. S1a). Input requires a subject x feature matrix where, in this case, features represent mean tau-PET signal within different ROIs. In addition, "severity scores", indicating different waypoints along the natural progression of ROI severity, must be provided. Whereas the choice of ROI constrains the spatial dimensions along which individuals may vary, the severity scores instead constrain the temporal dimension of variation. The total number of features is therefore represented by the product of N ROIs by N ROI-specific severity scores. A balance must thus be struck between resolution in the spatial and temporal dimensions, with respect to overall sample size.

Our discovery sample boasts scans from 1143 individuals, but even given our inclusion criteria, we expected from previous work[29] that the majority of individuals (50–60%) will have minimal tau binding (note that SuStaIn will automatically detect these individuals and exclude them from progression modeling). We therefore expect the modeling to be performed on a sample of closer to N~450–550. We therefore decided on ten different ROIs (spatial features), each with three severity scores (temporal dimension), totalling 30 features. Given an arbitrary rule of 10–20 observations per feature, 300–600 observations should provide sufficient power, and our sample size should therefore be sufficient.

For the ten spatial features, we opted for left and right lobar regions of interest: parietal, frontal, occipital, temporal and medial temporal lobe (MTL). This choice is justified as follows: i) previous imaging and pathology subtyping studies have revealed variation in AD pathology to often occur within specific lobes, e.g. limbic-predominant (MTL), MTL-sparing (parietal), posterior cortical atrophy (occipital), logopenic aphasia (temporal) and behavioral variant AD (perhaps frontal)[18]; ii) hemispheric laterality in AD is understudied,

perhaps due to pathological staining often occurring on single hemispheres. However, some laterality has been observed in AD clinical variants (i.e. lvPPA[15]) and may point to differing phenotypes in typical AD; iii) These lobar regions maintain some orthogonality to disease progression, as multiple lobes are involved in Braak stages IV - VI[8].

To define severity score cutoffs, we first sought to normalize SUVR values to account for regional differences in PET signal (due to nonuniformity of off-target binding, perfusion, etc. across the brain)[29]. Two-component Gaussian mixture models were used to define, for each ROI, a normal (Gaussian-shaped noise) and abnormal distribution. We then created tau Z-scores by normalizing all values using the mean of the normal distribution (Extended Data Fig. S1b). This procedure centered the Z-score values on the normal distribution to allow for more interpretable values (i.e. 2=2 SDs from normal), and also accounted for region-specific differences in normal and abnormal SUVR distributions. Uniform values of Z = 2, 5, 10 were arbitrarily chosen as severity score control points for all ROIs (Extended Data Fig. S1)B. However, analyses were also run with alternative z-score values, see the Replication Analysis section below.

The number of subtypes (i.e. distinct spatiotemporal progressions) was determined through cross-validation. Separately for each k=1–7 subtypes, 10-fold cross-validation was performed where, for each fold, SuStaIn was fit to 90% of the data, and this model was used to evaluate sample likelihood for the 10% left-out subjects. For each left-out set, model fit was evaluated using the cross-validation information criterion (CVIC; as described in [23]), as well as out-of-sample log-likelihood. In addition, we used the inner-fold SuStaIn model to assign all outer-fold individuals to a subtype, and we evaluated the probability of the maximum-likelihood subtype. In theory, a better fit model should produce more high probability assignments of left-out data, though more subtypes will also make assignment more challenging. k was chosen by evaluating these three metrics in concert (Extended Data Fig. S1c–e). CVIC increased significantly with increasing k, indicating better fit to the data as the number of subtypes increased, though the curve flattened somewhat after k=4 (Extended Data Fig. S1c). Similarly, log-likelihood increased indicating better model fit, up until k=4, after which no improvement was seen (Extended Data Fig. S1d). In contrast to these fit statistics, cross-validated maximum-likelihood subtype probability decreased with increasing k, indicating less-confident assignment of left-out data with more subtypes. This decline was steady, though the median probability dropped below 0.5 after k=4. Taken together, k=4 appeared to be the best solution to maximize model fit but minimize detriment to subtype confidence. We also noted that no subtypes after k=4 had more than one “parent” subtype. In other words, solutions 3 and 4 feature subtypes that were composed of multiple parent subtypes, whereas all solutions thereafter featured only subtypes that split off from a single parent subtype. This could be indicative of a certain level of hierarchical convergence at k=4 (Extended Data Fig. S1f).

Finally, SuStaIn was run on the whole sample with the selected k=4. Note that for model fitting, SuStaIn uses a uniform prior on disease subtype and stage (i.e. assumes all subtype and stage combinations equally likely). Note also that the model is initialized with an expectation-maximization algorithm, and therefore does not require a burn-in period.[23] The model was fit using 10000 Markov chain Monte Carlo (MCMC) iterations. SuStaIn

calculates the probability that each individual falls into each stage of each subtype, and individuals are assigned to their maximum likelihood subtype and stage. Note that individuals that do not express abnormal tau in any region are classified by SuStaIn as "Stage 0", and are not assigned to a subtype. The proportion of individuals classified into each subtype was quantified. We also stratified this quantification by clinical diagnosis, and to cohort to assess the frequency of subtypes in each contributing dataset. Finally, we quantified the proportion of subjects that did not fall well into any subtype (no subtype probability >50%).

Post-hoc subtype correction.

Manual inspection of subtype progressions suggested that the early stages of one subtype (S2: MTL-Sparing; see Results) were composed mostly of cognitively normal individuals with abnormally high tau-PET binding throughout the cortex, but little-to-no tau in typical early-mid AD regions, i.e. false (tau) positives. Specifically, these individuals showed elevated binding throughout the cortex, including sensorimotor and frontal regions (regions where tau typically accumulates only in the latest stages of AD[8]), but had low tau levels in the temporal lobes (Extended Data Fig. S1a). On an individual basis, such individuals showed tau-PET signal that was slightly but globally elevated, with several small "hotspots" distributed diffusely throughout frontal, parietal and occipital cortex. While it is unclear whether this elevated binding represents off-target binding, diffuse low-level target binding, or other methodological issues, consensus among co-authors was that these individuals were not consistent with an AD phenotype. We used Gaussian mixture modeling across all individuals as described in [29] to define the probability of abnormal tau-positivity in each of the left and right entorhinal cortex and precuneus, respectively. We then marked individuals who had <90% probability of tau in all four regions as low-probability tau individuals (T−). These individuals also underwent manual inspection. Next, we identified T- individuals in the MTL-Sparing subtype, finding 40.6% of this subtype was composed of this group, and all were classified as stage 5 (of 31) or below. Furthermore these individuals showed many other indications of being false (tau) positives: they had normal MMSE scores, were older, were less likely to be Aβ+ and less likely to be MCI or AD (Extended Data Fig. S2b,c). We assume SuStaIn appended this specific group of T- individuals to the MTL-Sparing subtype because the individuals i) had abnormally high tau in at least one ROI as per our calculations (even if that abnormal signal was not driven by pathology); ii) the abnormal tau was located mainly in the isocortex inclusive of the parietal lobe; iii) these individuals did not have elevated MTL binding. As SuStaIn is an unsupervised algorithm, the pathological MTL-sparing phenotype became conflated with this specific profile of T- individuals. To correct this issue, we converted all T- individuals classified as MTL-sparing to Subtype 0 for all further analysis.

Visualization of subtype-specific tau-PET patterns.

To visualize tau-PET patterns for each subtype, we calculated the mean tau Z-score for each Desikan-Killiany (freesurfer) atlas ROI. To visualize the progression of the subtype pattern across SuStaIn stages, for each subtype, we created mean images for all individuals falling into the following SuStaIn stage bins: 2–6, 7–11, 12–16, 17–21, 22–26. To deduce regions with relatively greater or less tau signal for each subtype, we created region-wise one-vs-all

ordinary least squares (OLS) linear models comparing regional tau in one subtype to all others. This analysis was performed to visualize subtype models inferred by SuStaIn using individual data, and to explore differences between subtypes. Each model included ROI tau Z-scores as the dependent variable, a one-hot dummy variable representing membership in the reference subtype, and SuStaIn stage as a covariate. These models were FDR-corrected for the number of comparisons (i.e. number of ROIs).

Subtype Characterization.

Several demographic, cognitive and genetic variables were available for nearly all individuals across the five cohorts in our main (discovery) cohort. These variables included clinical diagnosis (100%), age (99.8%), sex (100%), years of education (97.1%), mini mental state examination (MMSE) score (97.7%) and *APOE4* allele carriage (89.5%). Only the UCSF sample provided diagnoses of clinical AD variants such as PCA[16] and lvPPA[17]. In addition, most individuals underwent extensive cohort-specific cognitive batteries assessing multiple domains of cognition. In order to utilize this rich cognitive data, we created cognitive domain scores separately within each cohort by taking the mean of several z-scored tests within the following cognitive domains: memory, executive function, language and visuospatial function. Supplemental Table S5 indicates which cognitive tests were used in each cognitive domain score across each cohort. We calculated global cognition as the mean between the four domain scores. Finally, we additionally regressed global cognition out of each domain score to create “relative” cognitive domain scores. These scores are useful for assessing the degree of domain-specific impairment above and beyond global impairment. The various absolute and relative domain scores were then aggregated across all cohorts to maximize the sample size available for cognitive tests: memory (86.6%), language (81.3%), executive function (85.5%), visuospatial function (82.0%). While aggregating scores of different compositions across cohorts of different compositions presents a suboptimal solution, we rest on sample sizes and statistical correction helping to overcome these limitations.

Subtypes were statistically compared to one another, and to tau-negative (i.e. Stage 0) individuals, in order to determine subtype-specific characteristics. These analyses compared age, sex, education, APOE4 carriage, MMSE, global cognition, total tau, and total tau asymmetry. Comparisons between subtypes and Stage 0 individuals additionally included the four cognitive domain scores, while comparison between subtypes instead included the four “relative” cognitive domain scores. This statistical comparison involved three steps: 1) Comparison to tau-negative individuals: Tau-negative individuals were those characterized as “Subtype 0” by SuStaIn, i.e. those individuals that did not demonstrate any abnormal tau events. An OLS linear model was fit with each variable described above as the dependent variable, and with dummycoded subtype entered as the independent variable (with S0 as the reference subtype). The model also included age, sex, education, clinical status (CN, MCI, AD) and cohort as covariates (except when that covariate was the dependent variable). Model t- and p-values were stored for each model and the latter were FDR-corrected. 2) Comparison between subtypes. A one-vs-all approach was applied to subtyped individuals only to assess how different tau-progression subtypes differed from one another. Separately for each subtype, models were fit for each variable with a single dummy variable entered

indicating membership to that subtype. Models once again covaried for age, sex, education, clinical status (CN, MCI, AD), cohort, and, this time, SuStaIn stage. T and p values were stored, and the latter was FDR-corrected for the number of variables assessed. 3) Finally, each subtype was compared directly to each other subtype (i.e. one-vs-one comparison). OLS models were fit with dummy coded subtype variables as the dependent variable, cycling each subtype as the reference subtype. T and p values for each of these models were stored, and the latter was FDR-corrected for number of comparisons (i.e. number of dependent variables). These models were also adjusted for age, sex, education, clinical status (CN, MCI, AD), cohort and SuStaIn stage. For space reasons, the results of 3) are only visible in Extended Data Fig. S8.

All models were subjected to diagnostics to ensure our data fulfilled assumptions of OLS regression models. We found the residuals of all models to be normally distributed (Anderson-Darling tests $p>0.05$). Further, we found no strong evidence for autocorrelation (Durbin Watson test, $1.5 <$ all models < 2.5), outliers (Cooks distance of all subjects < 0.5), multicollinearity (variance inflation factor (VIF) for all covariates < 100; besides age [23–27], sex [8–12] and education [13–17], all VIF < 10) or heteroscedasticity (visual assessment of distribution around mean of residuals) in any of our models.

We also assessed the relationship between SuStaIn stage and two variables: age and MMSE. For these analyses, stage was correlated with age and MMSE, and the results were visualized across the whole sample and also stratified by subtype. As a post-hoc analysis, we separated individuals into different age groups: 65 or younger, and older than 65. We then reassessed age by SuStaIn stage correlations within each of these age groups.

Longitudinal MMSE data was also available for individuals from all cohorts, totalling 735 individuals with at least two timepoints. 195 individuals had an additional third timepoint, 29 had a fourth, and 3 had a fifth. Mean latest follow-up was 1.72 years from PET scan (sd = 0.64). Linear mixed effect models were used to assess difference in longitudinal MMSE change between subtypes. All models were fit using the lme4 library in R, using type-III sum of squares, unstructured covariance matrices, and Satterthwaite's approximation to calculate the denominator degrees of freedom for p-values. Models featured MMSE measurements as the dependent variable, interactions between time from baseline and dummy coded subtype variables as the independent variables of interest (cycling the reference subtype), subject ID as a random effect (allowing for random intercepts and slopes), and age, sex, education, cohort, dummy coded variables for MCI and AD, and SuStaIn stage as covariates of no interest. One vs all models were also fit for each subject using dummy coded subtype variables, and significant effects were reported. We additionally repeated the one vs. all subtype models within each cohort separately, and used this to calculate a meta-analysis by finding a weighted mean of the t-values and standard errors. Since this analysis was confirmatory, we used a one-tailed significance test to calculate the p-values.

Replication Analysis.

We performed two types of replication analysis. To ensure that our results were not driven by arbitrary z-score cutoffs, we reran models with completely different cutoffs. To ensure the

results were not driven by our sample or unique to the flortaucipir radiotracer, we repeated the analysis *de novo* in a separate cohort using a different tau-PET radiotracer.

SuStaIn require z-score values to anchor the psuedotime for each ROI (see section Subtype and Stage Inference above), and we chose values of 2,5,10 for all ROIs so as to not let any region bias or influence the model unduly, and to aid comparability across different regions. To ensure our results were not driven by this choice, we reran the model with a different set of z-score values chosen in a data-driven manner. The object was to allow the distribution of tau-PET data in each region to define natural waypoints in the data. For each input region, we fit Gaussian mixture models to the data, varying the number of components between 1 and 5. We used the model fit (AIC) to decide the optimal number of components for each region. Finally, we used five-fold cross-validation to determine the boundaries of these Gaussians to define anchors for each regions. We did this separately for each ROI, and as a result, different ROIs had different waypoints, and even different numbers of waypoints (Table S6). We then refit the SuStaIn model to the data and compared the results to the original model using spatial correlation (see below).

While the five cohorts from the main discovery sample all use flortaucipir as the tau-PET tracer, a sixth cohort (BioFINDER II; BF2) was available that instead used the RO948 radiotracer. While the two tracers have similar binding patterns, RO948 tends to have less off-target binding in the basal ganglia and better MTL signal, but frequently boasts high meningeal signal that can affect cortical SUVR measurement[53]. Because of these differences, we opted to leave BF2 out of the discovery sample, and instead use it as a replication cohort. This strategy allowed us to not only evaluate the stability of the subtypes in a new cohort, but also allowed us to evaluate whether the subtypes are robust to tau-PET radiotracer.

We reran SuStaIn *de novo* in the BF2 sample, using identical procedures to those described above (Methods: Subtype and Stage Inference), although using the discovery sample to inform the number of subtypes. The resulting subtypes were visualized and quantitatively assessed using spatial correlations. Specifically, mean within-subtype SUVRs were computed for each (freesurfer) ROI, and each discovery subtype ROI-vector was correlated to each replication (BF2) subtype ROI-vector. To account for whether different sample sizes contribute to differing results between the discovery and replication datasets, we performed a split-half analysis with the discovery sample. Specifically, we split the discovery sample in half and ran SuStaIn separately on each half, once again using the original discovery sample to inform the number of subtypes. We then compared each half, which had a sample size comparable to that of BF2, to the BF2 samples using spatial correlations.

Assessment of Longitudinal Stability.

Longitudinal PET data was available for individuals across all cohorts except for UCSF, totaling 519 individuals with at least two time points (mean follow-up time = 1.42, sd = 0.58, years). These longitudinal scans were used to validate the stability of subtypes over time, under the hypothesis that individuals should remain the same subtype, but should advance (or remain stable) in SuStaIn stage over time. ROIs for the longitudinal datasets

were Z-scored as described above, but using the cross-sectional cohort as the cohort for normalization. The SuStaIn model fitted to the cross-sectional dataset was used to infer subtype and stage of longitudinal data (all timepoints). Confusion matrices were built to assess subtype stability between baseline and first follow-up. Stability was calculated as proportion of individuals classified as the same subtype at follow-up, or who advanced from Stage 0 into a subtype, compared to the total number of individuals. Stability was also calculated excluding individuals who were classified as Stage 0 at baseline or follow-up. We also assessed the influence of subtype probability (i.e. the probability a subject falls into their given subtype) on individual subtype stability. Specifically, we compared the subtype probability of stable individuals to unstable individuals with a t-test. We additionally calculated overall model stability after excluding individuals using various subtype probability thresholds.

Subtype progression was assessed by observing change in SuStaIn stage over time in stable subtype individuals. We calculated the proportion of individuals who advanced, were stable, or regressed in disease stage over time, before and after accounting for model uncertainty. Specifically, while stages are generally characterized by advancing abnormality in a given region, uncertainty leads to some stages being characterized by probabilities of progressing abnormalities in more than one region. Therefore, individuals who advanced or regressed to a stage with event probabilities overlapping with their previous stage were considered to be stable. We also calculated annual change in SuStaIn stage by dividing total change in SuStaIn stage by number of years between baseline and final available timepoint. We used one-sample t-test against zero to assess whether significant change over time was observed across the whole sample, and within each subtype. We used ANOVAs and Tukey's post-hoc tests to assess differences in annual change in stage across the different subtypes. We also correlated annual change in stage with baseline stage, and with age.

Individual forecasting of longitudinal tau progression.

SuStaIn models spatiotemporal subtype progressions, but does so using only cross-sectional data. Therefore, longitudinal data can be used as "unseen" or "left-out" data, which can be used to test whether and to what extent individuals follow the trajectories predicted by SuStaIn. We accomplish this by using an individual's subtype and stage probability to generate a predicted second time point, and comparing the change between baseline and predicted follow-up to change between baseline and actual follow-up.

To do this, we first sought to predict the rate of change of stage for each individual. We trained a Lasso model to predict individual annualized change in SuStaIn stage (Δstage) using available data, and cross-validation to get out-of-sample predictions for each individual. Features included age, sex, education, amyloid status, APOE4 status, baseline stage MMSE and dummy coded variables for MCI, AD, and each subtype. For each fold, the model was trained on 90% of the data, and this model was used to predict Δstage in the 10% left out subjects. This process was repeated until predictions were made for each subject. The mean absolute error between the predicted and true Δstage was 0.91 stages/year. The predicted Δstage was used for subsequent aspects of the tau prediction. This is important,

as we are therefore minimizing the amount of longitudinal information leaking into the forecast.

Using this predicted Δstage, we were then able to predict an individual's stage at follow-up $k_{i,\text{new}}$ given any stage at baseline k, as $k_{i,\text{new}} = k + \Delta_{\text{stage}} t_i$, where t_i is the time between follow-up visits in years.

We can then evaluate the SuStaIn-predicted pattern of regional tau deposition at baseline $Y_{i,j}$ as

$$Y_{ij} = \sum_{c=1}^{C} \sum_{k=0}^{K} A_{j,c,k} P_{i,c,k}$$

or at follow-up $Z_{i,j}$ as

$$Z_{ij} = \sum_{c=1}^{C} \sum_{k=0}^{K} A_{j,c,k_{i,new}} P_{i,c,k}$$

where $A_{j,c,k}$ is an 'archetype' indicating the expected amount of tau deposition for biomarker j at stage k of subtype c and $P_{i,c,k}$ is the probability subject i is at stage k of subtype c. The archetype $A_{j,c,k}$ is estimated probabilistically from the Markov chain Monte Carlo (MCMC) samples of uncertainty provided by the SuStaIn algorithm, giving an average archetypal pattern accounting for the uncertainty in the progression pattern of each subtype. This means that each SuStaIn-predicted pattern $Y_{i,j}$ accounts for both uncertainty in the progression pattern of each subtype as well as uncertainty in the subtype and stage of each individual.

We can therefore represent the predicted change in tau as $Z_{i,j} - Y_{i,j}$. This vector represents the predicted change in tau Z-score in each of the ten spatial input features to SuStain (i.e. left and right temporal, parietal, occipital, frontal and medial temporal lobes). We evaluate the prediction by computing, for each individual, the correlation between the predicted and true regional tau change vectors. We evaluate the overall prediction across the whole sample, and within-subtypes, by comparing the average prediction against chance using one-sample t-tests against a correlation of zero.

Epidemic spreading model.

Perhaps the most prominent hypothesis of tau spread suggests tau oligomers spread directly from neuron to neuron through axonal connections. Under this hypothesis, diverse but systematic variations in tau spreading may be driven by variability in macroscale connectivity, network organization or vulnerable circuits. We test this idea by investigating whether a network diffusion model simulating tau spread through the human connectome can recapitulate the various subtype patterns discovered by SuStaIn. We have previously applied the epidemic spreading model (ESM)[58] to tau-PET data, showing diffusion of an agent through human connectivity data (measured with diffusion imaging-based tractography) can explain a majority of the variance of spatial tau patterns across a

population of individuals along the AD spectrum[29]. We here conduct the exact same analysis separately for each subtype identified through SuStaIn. We further allow the ESM to identify regional epicenters separately for each subtype, under the hypothesis that different subtype patterns may be driven by prominence of different cortico-limbic networks.

As described in [29], each tau-PET ROI was converted to tau-positive probabilities using mixture modeling. This process is similar to the Z-scoring procedure (Extended Data Fig. S1), though in this case, the probability that values fall onto the abnormal distribution is ascertained using five-fold cross-validation. These measures represent the probability that a given ROI exhibits tau in the abnormal range. Connectivity was measured from a dataset of 60 young healthy subjects from the CMU-60 DSI Template (http://www.psy.cmu.edu/coaxlab/data.html). Deterministic tractography was calculated for each individual by finding connections between ROIs using orientation distribution functions, and connectivity was measured using the anatomical connection density (ACD) metric[58]. Images were assessed for quality and connectomes were averaged across all 60 individuals. For each subtype separately, the ESM was fitted across all individuals, cycling through the average of each left-right pair of cortical ROIs (including hippocampus and amygdala, 33 pairs in total) as the model epicenter. The best fitting epicenter was selected by finding the model with the minimum mean euclidian distance between model predicted and observed tau spatial pattern across subjects. Model accuracy was represented as the r^2 between the mean observed ROI-level tau-PET probabilities and mean predicted probabilities across subjects. For each subtype, we compared the r^2 of the model using the best-fitting epicenter to the r^2 of models using an entorhinal epicenter. To gain confidence in the subject-specific epicenter, we bootstrapped the sample 1000 times and recomputed the best-fitting epicenter for each subtype. Epicenter probability was calculated as the frequency that an epicenter was selected as best epicenter across bootstrap samples.

We were additionally interested in how secondary seeding evolved over the course of each subtype progression. While the ESM is designed to ascertain the true pathological epicenter, the selected epicenter reflects the seeding point that best matches the spatial pattern of the dependent variable. As such, it is likely that “secondary epicenters” become important for disease spread at later disease stages. We binned individuals for each subtype into disease stage bins, as with Fig 1e. Individual epicenters were ascertained for each subject, and were aggregated based on lobe (MTL, temporal, frontal, parietal, occipital). We then calculated epicenter frequency among individuals in each stage bin for each subtype. This allowed us to track how the secondary epicenter evolve throughout the disease course for each subtype trajectory.

We repeated this same analysis with a different connectome based on rsfMRI connectivity from an elderly population, and using a higher-resolution atlas. The sample consisted of rsfMRI scans from 422 healthy elderly controls (166 Aβ-positive), 138 individuals with subjective cognitive decline but without objective impairment (48 Aβ-positive), and 83 Aβ-positive MCI patients. 57 individuals overlapped between this sample and the tau-PET discovery sample used for analysis. Functional data was processed using modified CPAC pipeline[60] involving slice time correction, bandpass filtering at 0.01–0.1 Hz, regression of motion, white matter and CSF signal, compcor physiological noise, and the 24 Friston

parameters. The timeseries also underwent adaptive censoring of volumes for which DVARS jumps above median+1.5*IQR were observed. Timeseries were averaged within ROIs of the 246-ROI Brainnetome cortical/subcortical atlas (https://atlas.brainnetome.org/), nodewise connectivity was calculated using either Fisher's Z transformed correlations or partial-correlation (see below). The ESM was fit using the bilateral A35/36r ROI as model epicenter, and the following combinations of parameters were varied: regions (cortical only or all regions), subject-base (Aβ-negative only vs. all subjects), density (edgewise thresholding at 0.02, 0.5, 0.1, 0.25, 1, or partial correlation with no thresholding, and normalization (whether connectivity matrices were normalized after density thresholding). The only parameter strongly affecting model performance was density threshold – partial correlation far outperformed all other conditions. Using all regions over only cortical regions bore slight advantages, as did using all subjects over only Aβ-negative. Normalization had no effect on outcomes. The best-fitting model was used for further analysis. The ESM was fit to each subject separately, and epicenter bootstrapping was performed, both as described above.

Extended Data

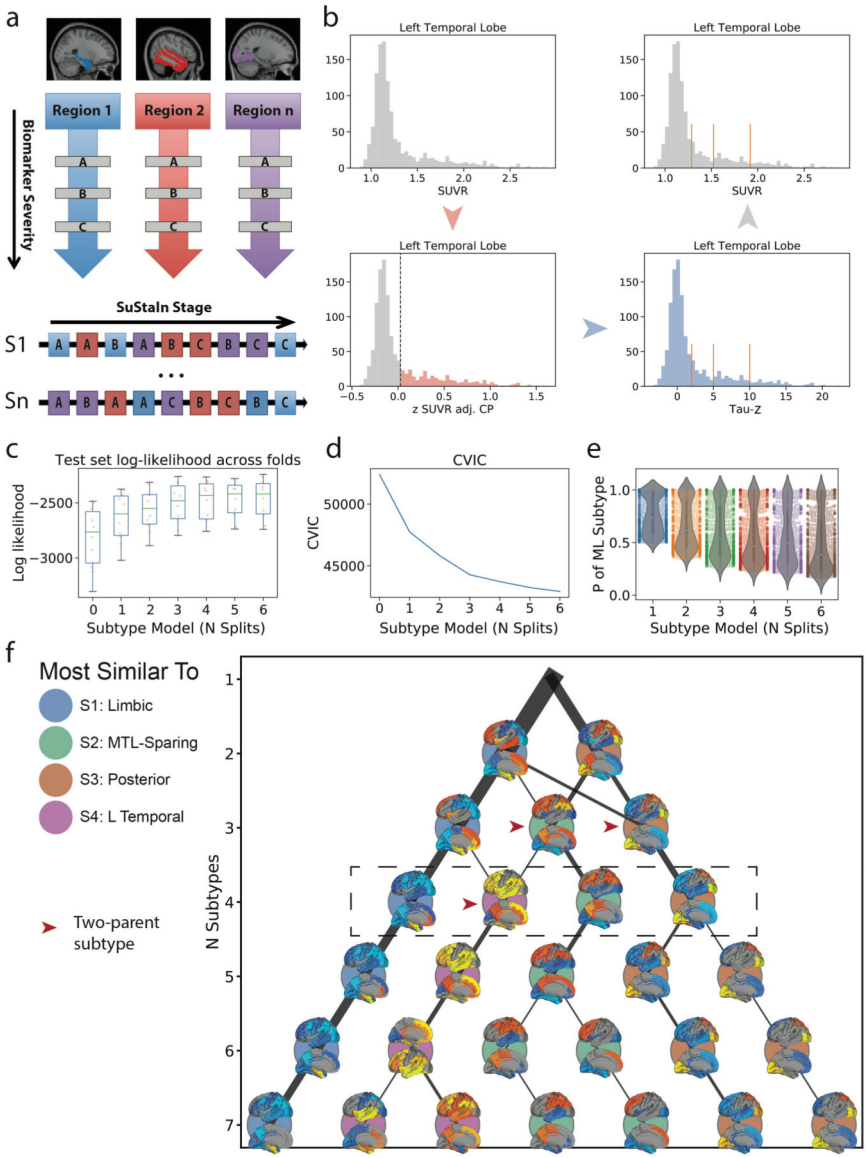

Figure S1.

Methodological details. a) SuStaIn requires both spatial (e.g. brain regions) and pseudotemporal (e.g. Z-score waypoints representing advancing biomarker severity) features as input. SuStaIn models linear change between waypoints across multiple biomarkers and uses k-means clustering to fit subtype trajectories representing distinct biomarker sequences. b) Each spatial feature was z-scored in order to derive interpretable waypoints. Example: (top left), SUVR distribution in the left temporal lobe. (bottom-left) Distribution of standardized residuals after regression of choroid plexus. Gaussian mixture-modeling identifies “normal” (grey) and “abnormal” (red) tau-PET values within this distribution. (bottom right) Mean and SD of “normal” distribution used to normalize the whole distribution, creating “Tau Z-scores”. Tau Z-scores of 2, 5 and 10 are used as waypoints. (top-right) Tau-z scores superimposed onto the original SUVR distribution. For each

subtype model (k=1–7), distribution of average negative log-likelihood, d) CVIC, and e) distribution of the probability of the maximum-likelihood subtype across cross-validation folds of left-out individuals. Higher log-likelihood, lower CVIC represents better model fit. f) Visualization of subtype solutions k=2–7. For each subtype, the rendered brains show significant regional tau difference between the subtype and all other subtypes in its solution. Connecting-line thickness indicates how many subjects are shared between a subtype and each subtype from its parent and child solutions. Circle color represents of the k=4 subtypes (outlined in the dashed box) each subtype is most similar to, in terms of the number of overlapping subjects. Red arrowheads indicate subtypes that were formed by pooling individuals from two different parent subtypes.

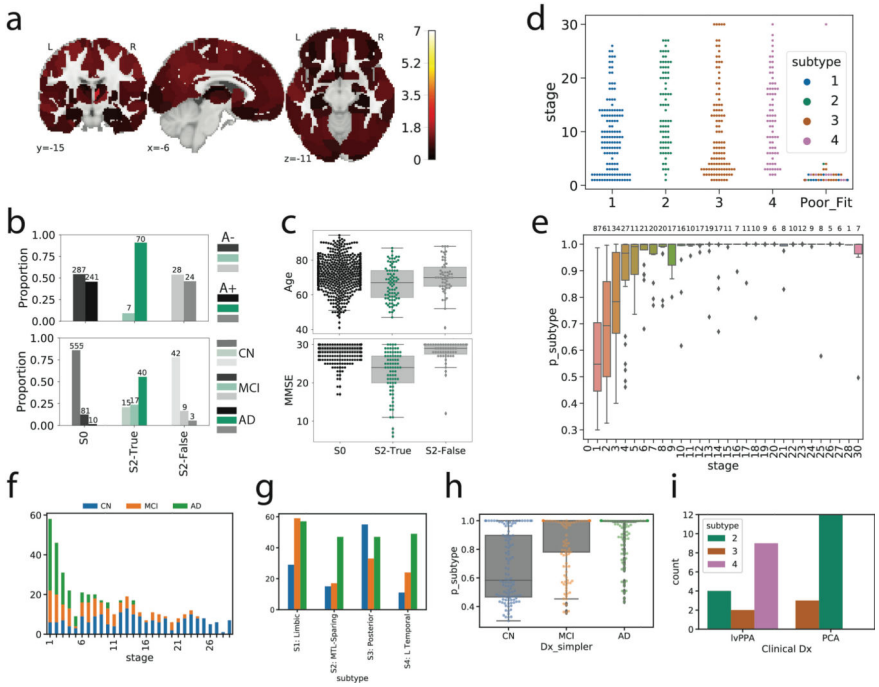

Figure S2.

Details of subtype assignment. a) Several individuals classified as S2 (MTL-Sparing) were found to be tau-negative (i.e. no significant tau in the entorhinal cortex or precuneus). Cortical rendering shows the overall mean tau Z-scores (see Fig S1b) of S2: False individuals. Slightly elevated signal was observed throughout the cortex (but not MTL areas), including in regions where pathological tau is not observed until late AD. b) Proportion of Aβ+ (top) and cognitively impaired (bottom) individuals in S2: False to other S2 individuals (S2: True) and tau-negative individuals (S0). Using, χ^2-tests with Tukey's posthoc correction, a higher proportion of S2: False and S0 individuals were Aβ-and cognitively impaired (ps<0.0001) than S2: True individuals, but did not differ significantly from one another (ps>0.05). c) Using ANOVAs with Tukey's posthoc correction, S0 and S2: False individuals were older and had higher MMSE scores than S2: True individuals, but did not differ from one another (ps>0.05). d) SuStaIn stage of all individuals stratified by subtype, with the poorly fitting subjects (those that had <0.5 probability of falling into any subtype) shown separately. All but one poorly fit subject exhibited very low SuStaIn

stages. e) Probability of maximum likelihood subtype is low at SuStaIn stage 1, but quickly increases with increasing SuStaIn stage. f) Distribution of clinical diagnoses across SuStaIn stages. g) Distribution of clinical diagnoses across subtypes. h) Distribution of maximum-likelihood subtype probabilities for each clinical diagnosis. i) Distribution of PCA and lvPPA subjects from the UCSF sample into each subtype

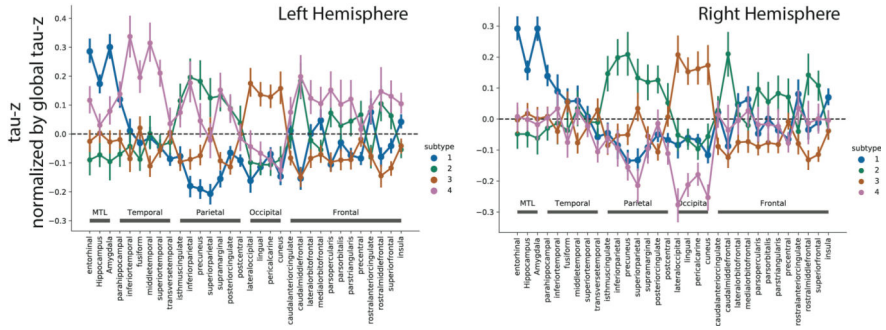

Figure S3.

Comparison of the mean tau-PET signal (tau-Z) across all ROIs, after adjustment for total cortical tau. A value of 0 represents a regional tau Z-score proportionate to the average cortical tau Z-score in that subtype. The left panel represents left hemisphere, the right panel represents right hemisphere. Confidence intervals represent standard error of the mean

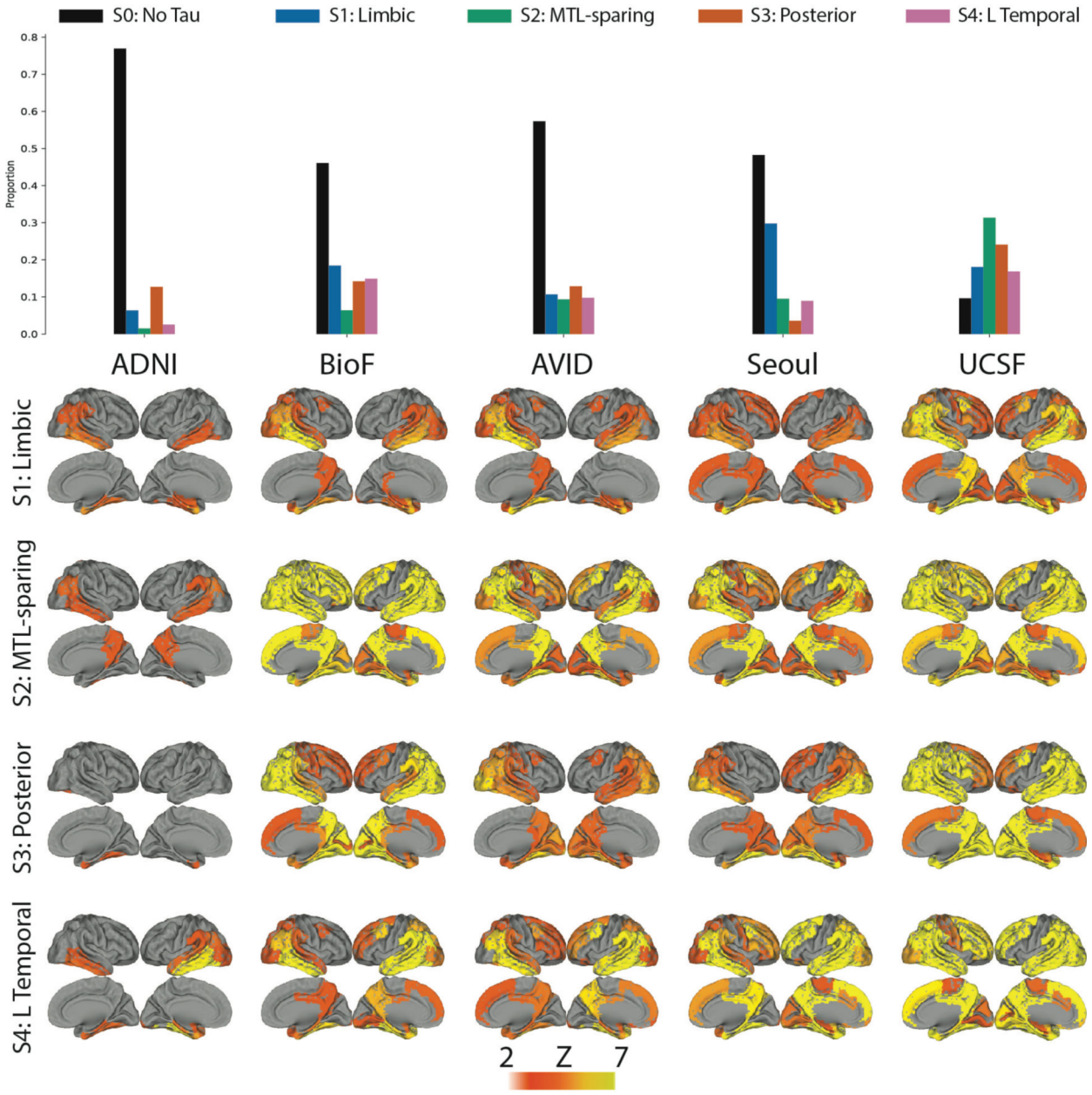

Figure S4.

All subtypes observable across all contributing cohorts. The top Figure shows the proportions of each subtype (plus S0) within each of the five cohorts. All cohorts included individuals from each subtype. The bottom shows the mean tau Z image of each subtypes in a given cohort. Variation can be observed across cohorts, particularly regarding phenotypic severity, but subtype patterns are fairly consistent.

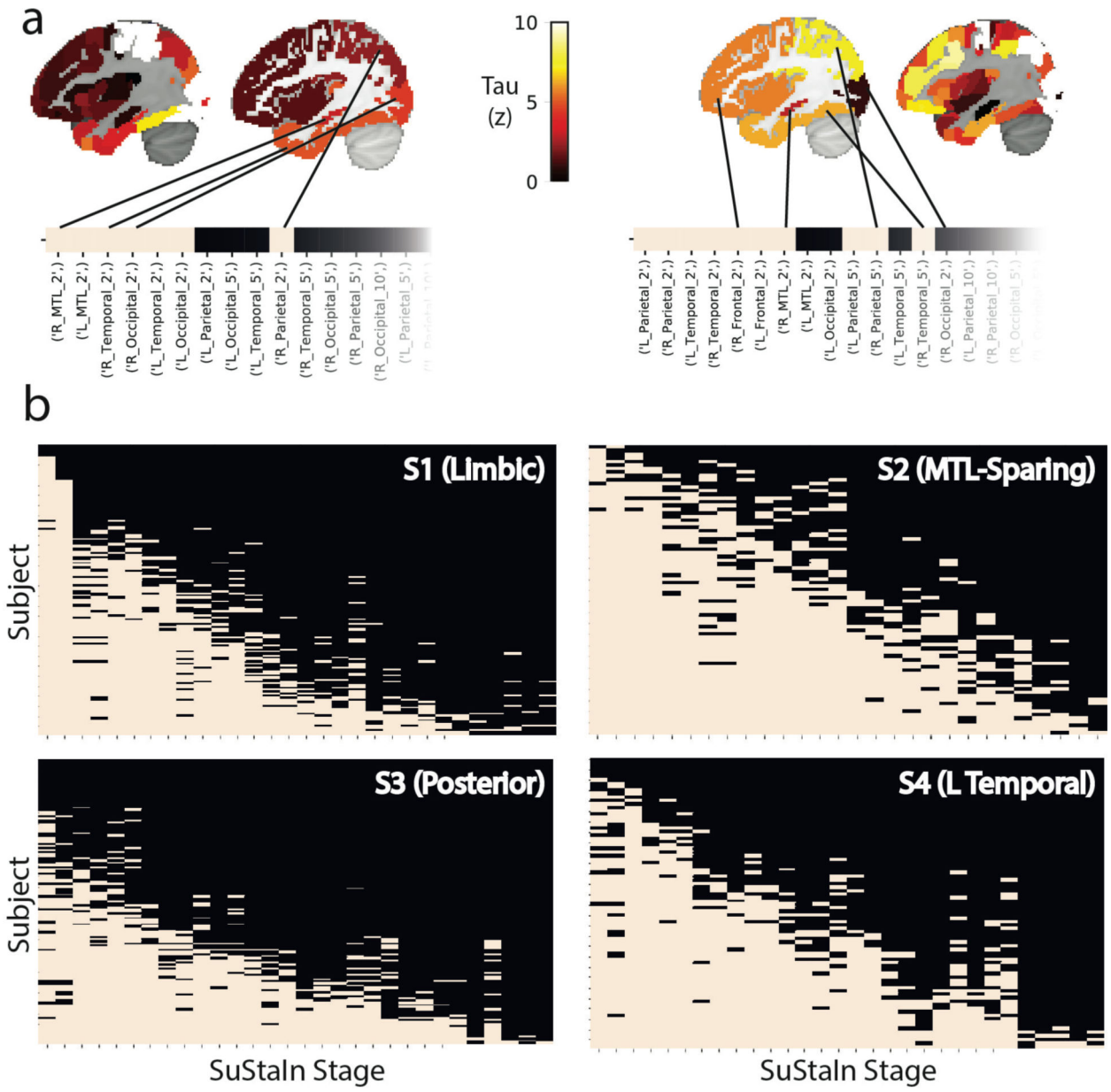

Figure S5.

Individual fit to stereotypical subtype progression. Progression plots are created for each subtyped individual based on their progression through the events specific to their subtype. The outer images show regional tau z scores (see Fig S1) for an S2 (left) and S3 (right) individual. This data is summarized in lobar ROI z-scores (inner images). In progression plots under the images, each box represents a biomarker event, tied to a SuStaIn stage. A SuStaIn stage represents tau reaching a given severity (w) score at a given region (see Fig S1). Filled (tan) boxes indicate an individual fulfills the criteria for that SuStaIn stage. An empty (black) box indicates an individual does not. Note that each subtype has a different event order. A stepwise progression plot is shown for each subtype. Each row represents an individual, and each column represents a SuStaIn stage. A perfect fit would be represented by an individual (row) having every box filled before a given stage, and no boxes filled after

it. The y-axis (subjects) are sorted from the least (top) to most (bottom) stages fulfilled. Across the population, this would be represented as a stepwise progression. Each subtype demonstrates a stepwise progression indicating good general fit. The average subject fit imperfection was 2.1 boxes.

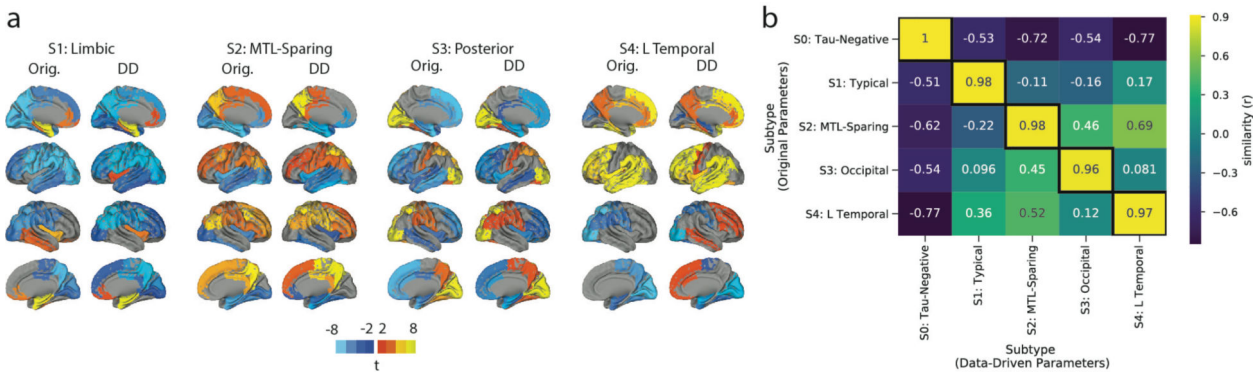

Figure S6.

SuStaIn creates nearly identical subtypes when initialized with different parameters (Table S5) see Methods: Replication Analysis). SuStaIn was rerun allowing a data-driven methodology to determine the number and value of z-score waypoints for each ROI. a) Qualitative contrasts of each subtype as defined using the original (Orig) parameters and the new data-driven (DD) parameters, where maps show regions significantly different between one subtype and all others (excluding S0) within the cohort (after FDR correction). b) Confusion matrix comparing subtypes identified in the original (orig) sample (y-axis), and subtypes separately identified in the data-driven parameter replication sample (x-axis). Values represent spatial correlation between average regional tau for each subtype. Values along the diagonal indicates similarity between the same subtype across both parameter sets.

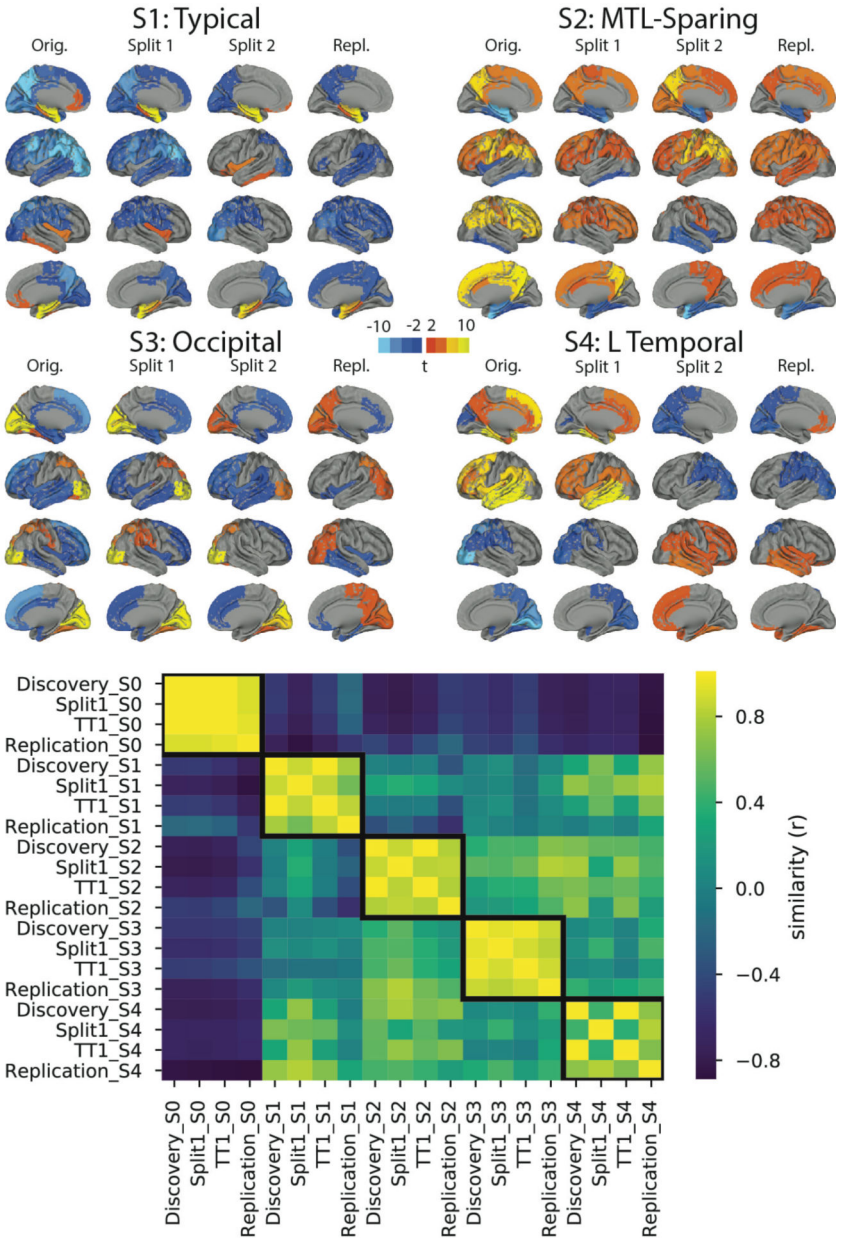

Figure S7.

Stability of subtypes across train-test split and replication datasets. (Top) Cortical renders showing, for each subtype across each dataset, regions with significantly different tau-PET signal compared to other within-dataset subtypes after FDR correction. Hot regions show greater tau-PET whereas cooler regions show lower signal. Remarkable similarity can be observed across subtypes, except S4, where lateralization switches from left to right. (Bottom) A heatmap showing similarity (spatial correlation) between subtypes across all four datasets. The diagonal represents the identity, whereas outlined boxes represent comparisons of the same subtype across cohorts.

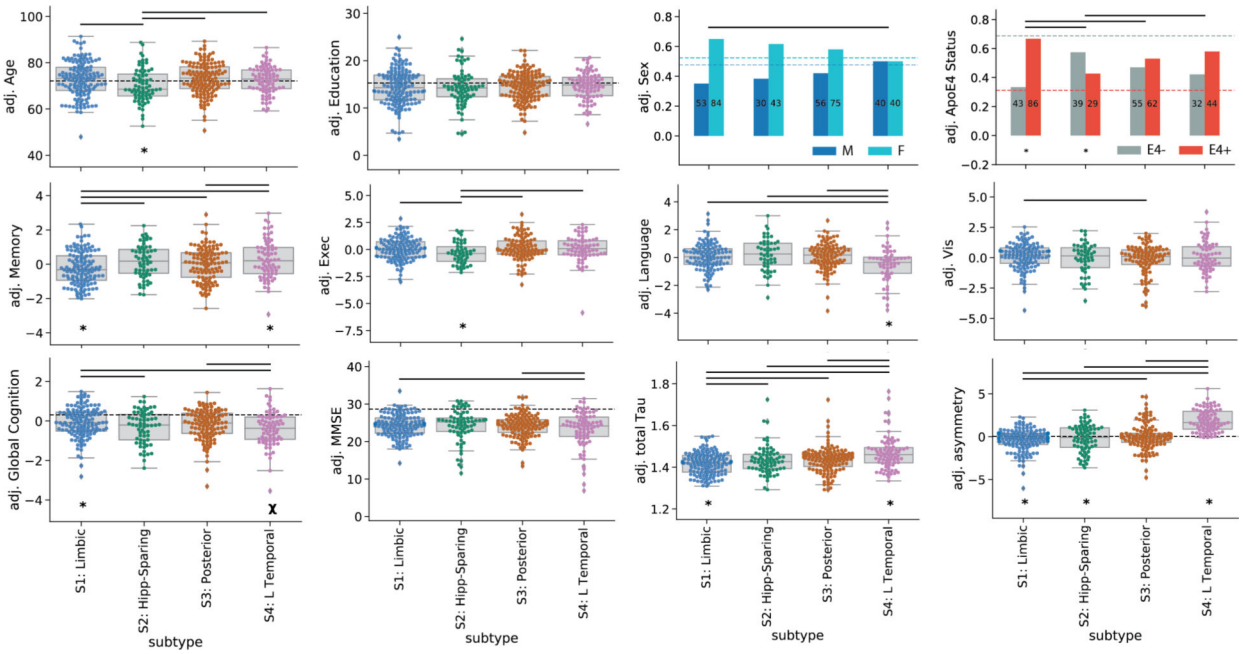

Figure S8.

Subtypes present with differing clinical profiles. For all plots, a * below a box indicates the subtype is significantly different (corrected $p<0.05$) from all other subtypes combined (one vs. all), while a χ represents a trend ($p<0.1$). Thick horizontal lines above boxes indicate significant ($p<0.05$) differences between two subtypes (one vs one). Dashed horizontal lines represent the mean of the S0 group (controlling for covariates), where relevant. All statistics are adjusted for demographics, disease status, cohort and SuStaIn stage. For boxplots, the center line=median, box=inner quartiles, whiskers=extent of data distribution except *=outliers

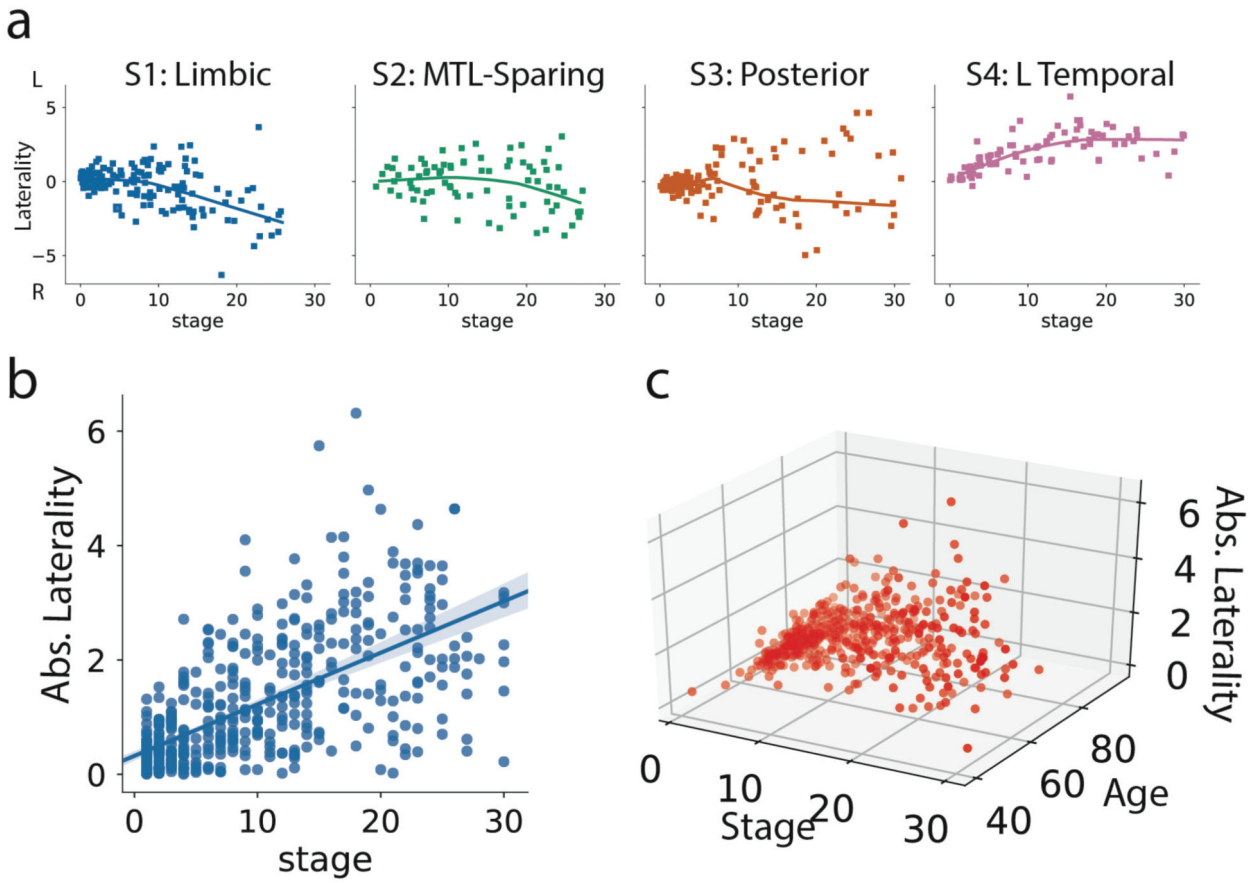

Figure S9.

Lateralization across disease progression as measured with SuStaIn stage. a) Tau lateralization was measured as the mean left to right ratio of tau Z scores for all ten tau features. Higher positive numbers represent greater left hemisphere tau lateralization, whereas lower negative numbers represent greater right hemisphere lateralization. The progression of laterality over SuStaIn stage was visualized for each subtype. Lateralization generally increased with increasing SuStaIn stage. In some subtypes (particularly S2 and S3), strong lateralization was seen in both hemispheres at later stages. b) The absolute (i.e. agnostic to hemisphere) lateralization (i.e. tau asymmetry) was visualized against SuStaIn stage, indicating a general increase in lateralization with more severe tau expression. c) A three-way relationship between age, SuStaIn stage and absolute lateralization is visualized, indicating these relationships covary but are independent of one another.

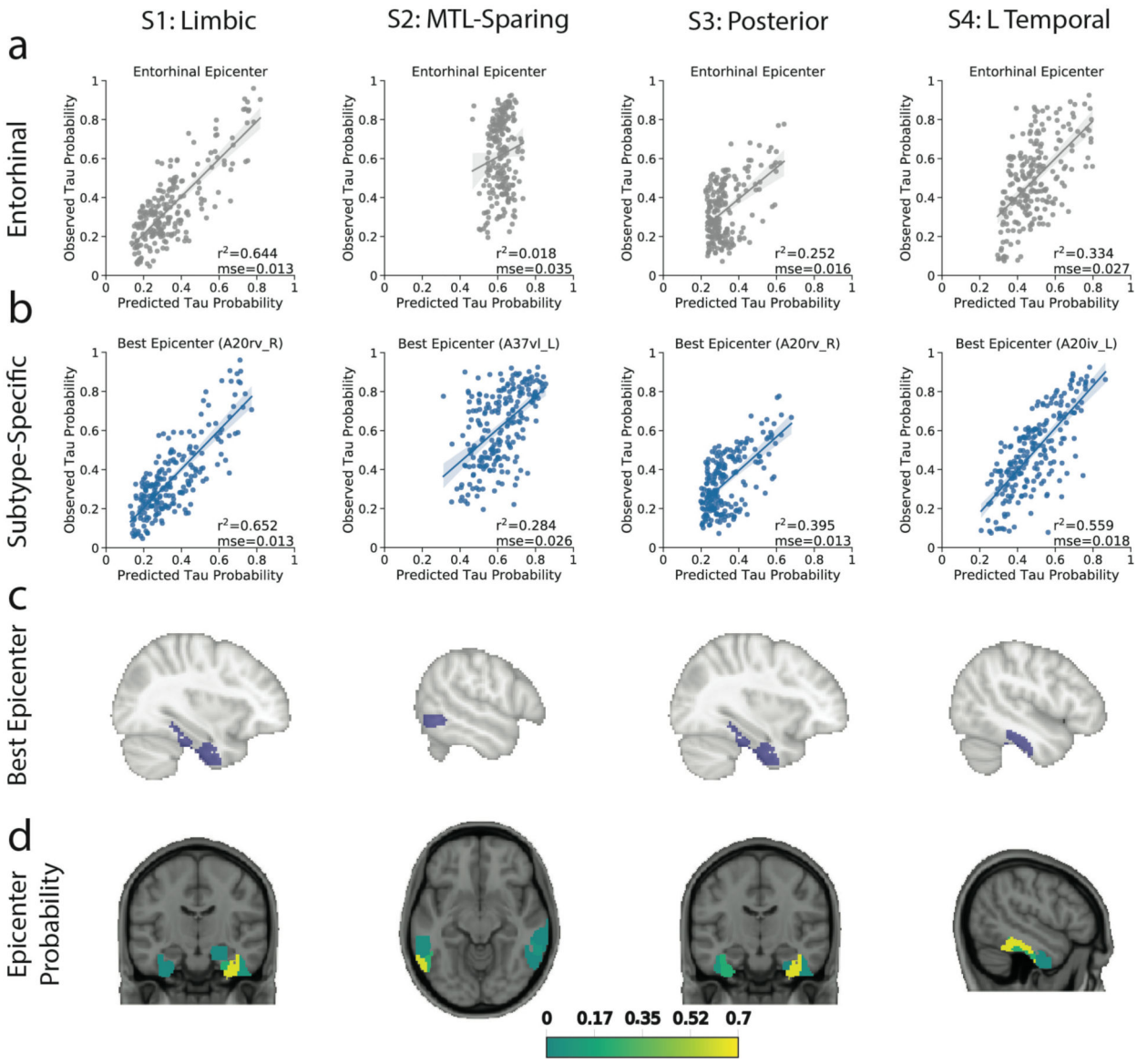

Figure S10.

Replication of subtype-specific epidemic spreading model. We repeated analyses from Fig. 4, this time using functional connectivity from a sample of elderly healthy and MCI individuals, over a higher-resolution cortical atlas, as the connectome input to the model. The ESM was fit separately for each subtype; once using an entorhinal cortex epicenter [a), gray], and once with a subtype-specific best-fitting epicenter [b), blue]. For each plot, each dot represents a region. The x-axis represents the mean simulated tau-positive probabilities across the population, while the y-axis represents the mean observed tau-positive probability. Each column represents a subtype. c) Visualization of the best-fitting epicenter selected by the model. d) For each subtype, the probability that each region is the best fitting epicenter for that subtype, based on bootstrap resampling.

Supplementary Material

Refer to Web version on PubMed Central for supplementary material.

Acknowledgements

The authors would like to acknowledge Drs. Mallar Chakravarty, Bratislav Misic, Pierre Bellec, Pedro Rosa-Neto, Alain Dagher, Edith Hamel and William Seeley for feedback during the composition of this manuscript. JWV acknowledges support from the government of Canada through a tri-council Vanier Canada Graduate Doctoral fellowship, from the McGill Centre for Integrative Neuroscience and the Healthy Brains, Healthy Lives initiative, and by the NIH (T32MH019112). ALY is supported by an MRC Skills Development Fellowship. NPO is a UKRI Future Leaders Fellow (MR/S03546X/1). NPO and DCA acknowledge support from the UK National Institute for Health Research University College London Hospitals Biomedical Research Centre, and DCA acknowledges support from EPSRC grant EP/M020533/1. MJG is supported by the “Miguel Servet” program [CP19/00031] and a research grant [PI20/00613] of the Instituto de Salud Carlos III-Fondo Europeo de Desarrollo Regional (ISCIII-FEDER). Author RL acknowledges support from the NIH (K99AG065501). This project has received funding from the European Union’s Horizon 2020 research and innovation programme under grant agreement No. 666992. The BioFINDER studies are supported by the Swedish Research Council (2016–00906), the Knut and Alice Wallenberg foundation (2017–0383), the Marianne and Marcus Wallenberg foundation (2015.0125), the Strategic Research Area MultiPark (Multidisciplinary Research in Parkinson’s disease) at Lund University, the Swedish Alzheimer Foundation (AF-939932), the Swedish Brain Foundation (FO2019–0326), The Parkinson foundation of Sweden (1280/20), the Skåne University Hospital Foundation (2020-O000028), Regionalt Forskningsstöd (2020–0314) and the Swedish federal government under the ALF agreement (2018-Projekt0279). The Tau PET study in Gangnam Severance Hospital was supported by a grant from Basic Science Research Program through the National Research Foundation of Korea (NRF) funded by the Ministry of Education (NRF2018R1D1A1B07049386 & NRF2020R1F1A1076154) and a grant of the Korea Health Technology R&D Project through the Korea Health Industry Development Institute (KHIDI) funded by the Ministry of Health & Welfare, Republic of Korea (Grant number: HI18C1159). We would additionally like to thank Bruce Miller, Howie Rosen, Marilu Gorno Tempini and Bill Jagust for supporting the UCSF tau-PET studies, which were funded through the following sources: NIA R01 AG045611 (Rabinovici), P50 AG23501 (Miller, Rosen, Rabinovici), P01 AG019724 (Miller, Rosen, Rabinovici). The precursor of 18F-flortaucipir was provided by AVID radiopharmaceuticals. The precursor of 18F-flutemetamol was sponsored by GE Healthcare. The precursor of 18F-RO948 was provided by Roche. Data collection and sharing for this project was funded by the Alzheimer’s Disease Neuroimaging Initiative (ADNI) (National Institutes of Health Grant U01 AG024904) and DOD ADNI (Department of Defense award number W81XWH-12–2-0012). ADNI is funded by the National Institute on Aging, the National Institute of Biomedical Imaging and Bioengineering, and through generous contributions from the following: AbbVie, Alzheimer’s Association; Alzheimer’s Drug Discovery Foundation; Araclon Biotech; BioClinica, Inc.; Biogen; Bristol-Myers Squibb Company; CereSpir, Inc.; Cogstate; Eisai Inc.; Elan Pharmaceuticals, Inc.; Eli Lilly and Company; EuroImmun; F. Hoffmann-La Roche Ltd and its affiliated company Genentech, Inc.; Fujirebio; GE Healthcare; IXICO Ltd.;Janssen Alzheimer Immunotherapy Research Development, LLC.; Johnson Johnson Pharmaceutical Research Development LLC.; Lumosity; Lundbeck; Merck Co., Inc.;Meso Scale Diagnostics, LLC.; NeuroRx Research; Neurotrack Technologies; Novartis Pharmaceuticals Corporation; Pfizer Inc.; Piramal Imaging; Servier; Takeda Pharmaceutical Company; and Transition Therapeutics. The Canadian Institutes of Health Research is providing funds to support ADNI clinical sites in Canada. Private sector contributions are facilitated by the Foundation for the National Institutes of Health (www.fnih.org). The grantee organization is the Northern California Institute for Research and Education, and the study is coordinated by the Alzheimer’s Therapeutic Research Institute at the University of Southern California. ADNI data are disseminated by the Laboratory for Neuro Imaging at the University of Southern California. Finally, we would like to all participants of this study, and families and care-givers of included patients, for their support in volunteering data for this study.

Competing interests

MJP and MDD are employees of Avid Radiopharmaceuticals, a wholly owned subsidiary of Eli Lilly and Company and are minor stockholders in Eli Lilly. OH has acquired research support (for the institution) from AVID Radiopharmaceuticals, Biogen, Eli Lilly, Eisai, GE Healthcare, Pfizer, and Roche. In the past 2 years, he has received consultancy/speaker fees from AC Immune, Alzpath, Biogen, Cerveau and Roche. The remaining authors declare no competing interests.

Data Availability statement

Tau-PET data contributing to this study was sourced from six different cohorts. One of them, ADNI, is a public access dataset and can be obtained through an application at http://

adni.loni.usc.edu/. Data from the other datasets are not publicly available for download, but access requests can be made to the respective study Investigators: BioFINDER 1,2 – Oskar Hansson; UCSF Memory and Aging Center – Gil D Rabinovici; Gangnam Severence Hospital, Seoul – Chul Hyoung Lyoo; AVID Radiopharmaceuticals – Michael J Pontecorvo, Michael D Devous. Additionally, CMU60 DTI data used to create template DTI connectomes are publicly available, and can be accessed at https://www.cmu.edu/dietrich/psychology/cognitiveaxon/data.html.

References

1. Hurd MD, Martorell P, Delavande A, Mullen KJ & Langa KM Monetary Costs of Dementia in the United States. N. Engl. J. Med. 368, 1326–1334 (2013). [PubMed: 23550670]
2. Alafuzoff I et al. Staging of Neurofibrillary Pathology in Alzheimer's Disease: A Study of the BrainNet Europe Consortium. Brain Pathol. 0, 080509082911413-??? (2008).
3. Hyman BT et al. National Institute on Aging-Alzheimer's Association guidelines for the neuropathologic assessment of Alzheimer's disease. Alzheimer's Dement. 8, 1–13 (2012). [PubMed: 22265587]
4. Hardy J & Selkoe DJ The Amyloid Hypothesis of Alzheimer's Disease: Progress and Problems on the Road to Therapeutics. Science (80-.). 297, 353–356 (2002).
5. Jack CR et al. Tracking pathophysiological processes in Alzheimer's disease: An updated hypothetical model of dynamic biomarkers. Lancet Neurol. 12, 207–216 (2013). [PubMed: 23332364]
6. La Joie R et al. Prospective longitudinal atrophy in Alzheimer's disease correlates with the intensity and topography of baseline tau-PET. Sci. Transl. Med. 12, 1–13 (2020).
7. Bejanin A et al. Tau pathology and neurodegeneration contribute to cognitive impairment in Alzheimer ' s disease. 1–15 (2017) doi:10.1093/brain/awx243.
8. Braak H & Braak E Neuropathological stageing of Alzheimer-related changes. Acta Neuropathol. 82, 239–59 (1991). [PubMed: 1759558]
9. Braak H, Alafuzoff I, Arzberger T, Kretzschmar H & Tredici K Staging of Alzheimer disease-associated neurofibrillary pathology using paraffin sections and immunocytochemistry. Acta Neuropathol. 112, 389–404 (2006). [PubMed: 16906426]
10. Schöll M et al. PET Imaging of Tau Deposition in the Aging Human Brain. Neuron (2016) doi:10.1016/j.neuron.2016.01.028.
11. Schwarz AJ et al. Regional profiles of the candidate tau PET ligand 18 F-AV-1451 recapitulate key features of Braak histopathological stages. Brain aww023 (2016) doi:10.1093/brain/aww023.
12. Murray ME et al. Neuropathologically defined subtypes of Alzheimer's disease with distinct clinical characteristics: A retrospective study. Lancet Neurol. 10, 785–796 (2011). [PubMed: 21802369]
13. Whitwell JL et al. Neuroimaging correlates of pathologically defined subtypes of Alzheimer's disease: A case-control study. Lancet Neurol. 11, 868–877 (2012). [PubMed: 22951070]
14. Ferreira D, Nordberg A & Westman E Biological subtypes of Alzheimer's disease: a systematic review and meta-analysis. Neurology 0, under-review (2020).
15. Ossenkoppele R et al. Tau PET patterns mirror clinical and neuroanatomical variability in Alzheimer's disease. Brain 139, 1551–1567 (2016). [PubMed: 26962052]
16. Crutch SJ et al. Consensus classification of posterior cortical atrophy. Alzheimer's Dement. 13, 870–884 (2017). [PubMed: 28259709]
17. Gorno-Tempini ML et al. Classification of primary progressive aphasia and its variants. Neurology 76, 1006–1014 (2011). [PubMed: 21325651]
18. Ossenkoppele R et al. The behavioural/dysexecutive variant of Alzheimer's disease: Clinical, neuroimaging and pathological features. Brain 138, 2732–2749 (2015). [PubMed: 26141491]
19. Drummond E et al. Proteomic differences in amyloid plaques in rapidly progressive and sporadic Alzheimer's disease. Acta Neuropathol. 133, 933–954 (2017). [PubMed: 28258398]

20. Crist AM et al. Leveraging selective hippocampal vulnerability among Alzheimer's disease subtypes reveals a novel tau b i nding partner SERPINA 5. bioRxiv 2020.12.18.423469 (2020) doi:10.1101/2020.12.18.423469.
21. Risacher SL et al. Alzheimer disease brain atrophy subtypes are associated with cognition and rate of decline. Neurology 89, 2176–2186 (2017). [PubMed: 29070667]
22. Ossenkoppele R et al. Distinct tau PET patterns in atrophy-defined subtypes of Alzheimer's disease. Alzheimer's Dement. 16, 335–344 (2020). [PubMed: 31672482]
23. Young AL et al. Uncovering the heterogeneity and temporal complexity of neurodegenerative diseases with Subtype and Stage Inference. Nat. Commun. 9, 4273 (2018). [PubMed: 30323170]
24. Dong A et al. Heterogeneity of neuroanatomical patterns in prodromal Alzheimer's disease: links to cognition, progression and biomarkers. Brain 140, 735–747 (2017). [PubMed: 28003242]
25. Noh Y et al. Anatomical heterogeneity of Alzheimer disease: based on cortical thickness on MRIs. Neurology 83, 1936–44 (2014). [PubMed: 25344382]
26. Tam A et al. A highly predictive signature of cognition and brain atrophy for progression to Alzheimer's dementia. Gigascience 8, 1–16 (2019).
27. Vogel JW et al. Data-driven approaches for tau-PET imaging biomarkers in Alzheimer's disease. Hum. Brain Mapp. 40, 638–651 (2019). [PubMed: 30368979]
28. Leuzy A et al. Diagnostic Performance of RO948 F 18 Tau Positron Emission Tomography in the Differentiation of Alzheimer Disease from Other Neurodegenerative Disorders. JAMA - Neurol. 1–12 (2020) doi:10.1001/jamaneurol.2020.0989.
29. Vogel JW et al. Spread of pathological tau proteins through communicating neurons in human Alzheimer's disease. Nat. Commun. 11, 2612 (2020). [PubMed: 32457389]
30. Marshall GA, Fairbanks LA, Tekin S, Vinters HV & Cummings JL Early-onset Alzheimer's disease is associated with greater pathologic burden. J. Geriatr. Psychiatry Neurol. 20, 29–33 (2007). [PubMed: 17341768]
31. Whitwell JL et al. The role of age on tau PET uptake and gray matter atrophy in atypical Alzheimer's disease. Alzheimer's Dement. 15, 675–685 (2019). [PubMed: 30853465]
32. Pontecorvo MJ et al. A multicentre longitudinal study of flortaucipir (18F) in normal ageing, mild cognitive impairment and Alzheimer's disease dementia. Brain 142, 1723–1735 (2019). [PubMed: 31009046]
33. Jack CR et al. Predicting future rates of tau accumulation on PET. Brain 143, 3136–3150 (2020). [PubMed: 33094327]
34. La Joie R et al. Association of APOE4 and clinical variability in Alzheimer disease with the pattern of tauand amyloid-PET. Neurology 10.1212/WNL.0000000000011270 (2020) doi:10.1212/wnl.0000000000011270.
35. Dujardin S et al. Tau molecular diversity contributes to clinical heterogeneity in Alzheimer's disease. Nat. Med. (2020) doi:10.1038/s41591-020-0938-9.
36. Aoyagi A et al. Aβ and tau prion-like activities decline with longevity in the Alzheimer's disease human brain. Sci. Transl. Med. 11, 1–14 (2019).
37. Koedam ELGE et al. Early-Versus Late-Onset Alzheimer's Disease: More than Age Alone. J. Alzheimer's Dis. 19, 1401–1408 (2010). [PubMed: 20061618]
38. Sun N, Mormino EC, Chen J, Sabuncu MR & Yeo BTT Multi-modal latent factor exploration of atrophy, cognitive and tau heterogeneity in Alzheimer's disease. Neuroimage 201, (2019).
39. Franzmeier N et al. Patient-centered connectivity-based prediction of tau pathology spread in Alzheimer's disease. Sci. Adv 6, eabd1327 (2020). [PubMed: 33246962]
40. Mukaetova-Ladinska EB et al. Regional Distribution of Paired Helical Filaments and Normal Tau Proteins in Aging and in Alzheimer's Disease with and without Occipital Lobe Involvement. Dement. Geriatr. Cogn. Disord. 3, 61–69 (1992).
41. McKee AC et al. Visual Association Pathology in Preclinical Alzheimer Disease. J. Neuropathol. Exp. Neurol. 65, 621–630 (2006). [PubMed: 16783172]
42. Pikkarainen M, Kauppinen T & Alafuzoff I Hyperphosphorylated Tau in the Occipital Cortex in Aged Non-demented Subjects. J. Neuropathol. Exp. Neurol. 68, 653–660 (2009). [PubMed: 19458543]

43. Hanna Al-Shaikh F. S. et al. Selective Vulnerability of the Nucleus Basalis of Meynert among Neuropathologic Subtypes of Alzheimer Disease. JAMA Neurol. 32224, 225–233 (2019).
44. Machado A et al. The cholinergic system in subtypes of Alzheimer's disease: an in vivo longitudinal MRI study. Alzheimers. Res. Ther. 12, 51 (2020). [PubMed: 32375872]
45. Rogalski E, Johnson N, Weintraub S & Mesulam M Increased Frequency of Learning Disability in Patients With Primary Progressive Aphasia and Their First-Degree Relatives. Arch. Neurol. 65, 1–7 (2008).
46. Ossenkoppele R et al. Discriminative accuracy of [18F]flortaucipir positron emission tomography for Alzheimer disease vs other neurodegenerative disorders. JAMA J. Am. Med. Assoc. 320, 1151–1162 (2018).
47. Miller ZA et al. Cortical developmental abnormalities in logopenic variant primary progressive aphasia with dyslexia. Brain Commun. 1–8 (2019) doi:10.1093/braincomms/fcz027.
48. Hyman BT Tau propagation, different tau phenotypes, and prion-like properties of tau. Neuron 82, 1189–1190 (2014). [PubMed: 24945760]
49. He Z et al. Transmission of tauopathy strains is independent of their isoform composition. Nat. Commun. 11, (2020).
50. Leng K et al. Molecular characterization of selectively vulnerable neurons in Alzheimer's Disease. (2020).
51. Lemoine L, Leuzy A, Chiotis K, Rodriguez-Vieitez E & Nordberg A Tau positron emission tomography imaging in tauopathies: The added hurdle of off-target binding. Alzheimer's Dement. Diagnosis, Assess. Dis. Monit. 10, 232–236 (2018).
52. Baker SL, Harrison TM, Maaß A, La Joie R & Jagust W Effect of off-target binding on 18 F-Flortaucipir variability in healthy controls across the lifespan. J. Nucl. Med. jnumed.118.224113 (2019) doi:10.2967/jnumed.118.224113.
53. Smith R et al. Head-to-head comparison of tau positron emission tomography tracers [18F]flortaucipir and [18F]RO948. Eur. J. Nucl. Med. Mol. Imaging 47, 342–354 (2020). [PubMed: 31612245]
54. Fleisher AS et al. Positron Emission Tomography Imaging with [18F]flortaucipir and Postmortem Assessment of Alzheimer Disease Neuropathologic Changes. JAMA Neurol. 77, 829–839 (2020). [PubMed: 32338734]
55. Lowe VJ et al. Tau-positron emission tomography correlates with neuropathology findings. Alzheimer's Dement. 16, 561–571 (2020). [PubMed: 31784374]
56. Soleimani-Meigooni DN et al. 18F-flortaucipir PET to autopsy comparisons in Alzheimer's disease and other neurodegenerative diseases. Brain 143, (2020).
57. Smith R, Wibom M, Pawlik D, Englund E & Hansson O Correlation of in Vivo [18 F]Flortaucipir with Postmortem Alzheimer Disease Tau Pathology. JAMA Neurol 76, 310–317 (2019). [PubMed: 30508025]

Methods References

58. Iturria-Medina Y, Sotero RC, Toussaint PJ & Evans AC Epidemic Spreading Model to Characterize Misfolded Proteins Propagation in Aging and Associated Neurodegenerative Disorders. PLoS Comput. Biol. 10, (2014).
59. Cho H et al. Predicted sequence of cortical tau and amyloid-β deposition in Alzheimer disease spectrum. Neurobiol. Aging 68, 76–84 (2018). [PubMed: 29751288]
60. Craddock C, Sikka S, Cheung B, Khanuja R, Ghosh SS, Yan C, Li Q, Lurie D, Vogelstein J, Burns R, S. C & Mennes M, Kelly C, Di Martino A, F C. and M. M Towards Automated Analysis of Connectomes: The Configurable Pipeline for the Analysis of Connectomes (C-PAC). Front. Neuroinform. 7, (2013).

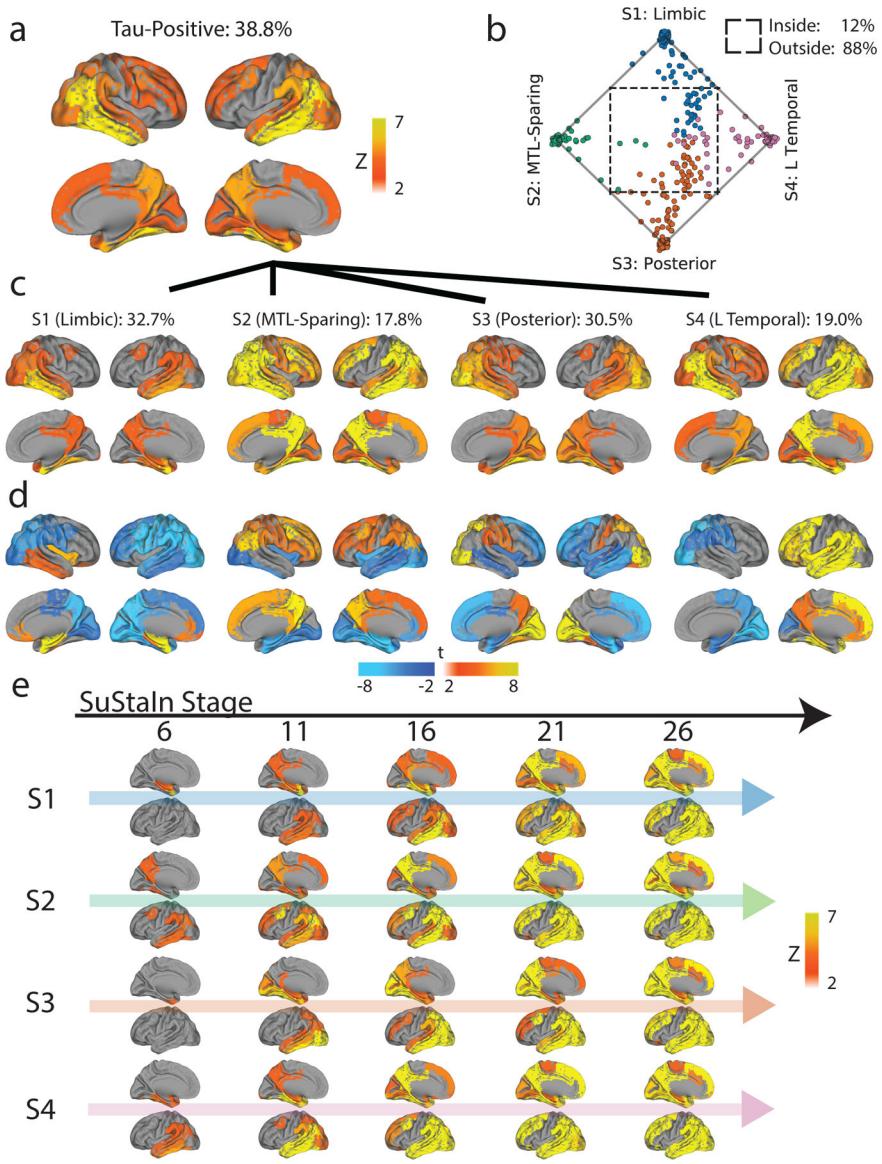

Figure 1.

Spatiotemporal subtypes of tau progression. A) Tau-PET pattern of tau-positive (subtyped) individuals. B) Quarternary plot showing probability each individual is classified as each subtype. Dots are labeled by final subtype classification: S1 (blue), S2 (green), S3 (orange) or S4 (pink). Inset box shows individuals that had a probability < 0.5 to be classified as any of the four subtypes (i.e. showing poor fit). C) Average tau-PET pattern for each subtype. The colorbar is the same as Panel A. D) Regions showing significant difference between one subtype and all other subtypes using OLS linear models adjusting for SuStaIn stage, after FDR correction. E) Progression of each subtype through SuStaIn stages. Each image is a mean of individuals classified at the listed stage and up to four stages lower. Only the left hemisphere is shown.

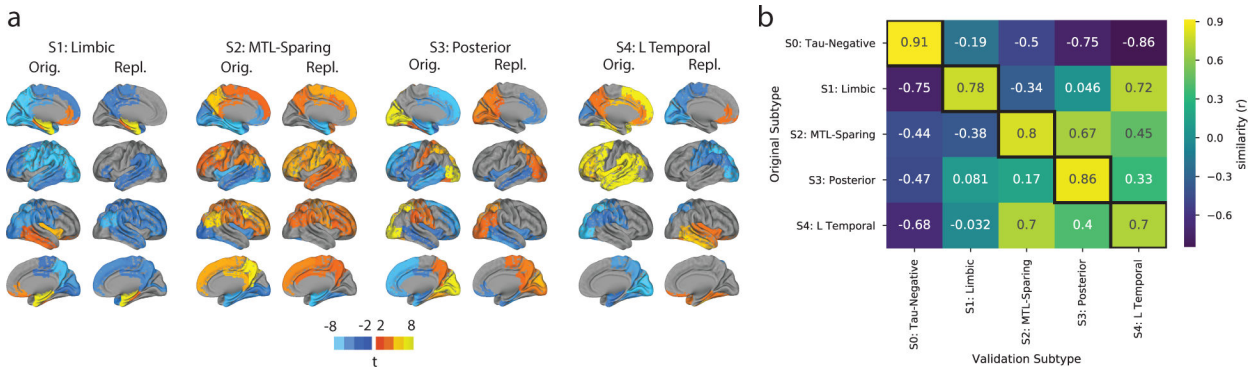

Figure 2.

Subtype stability: AD spatiotemporal subtypes replicate in another cohort using a different PET tracer. A) For both the discovery (Orig) and replication (Repl) cohorts, maps showing regions significantly different between one subtype and all others (excluding S0) within the cohort (after FDR correction). Similar spatial patterns were observed, except for a reversed pattern in S4. B) Confusion matrix comparing subtypes identified in the original (discovery) sample (y-axis), and subtypes separately identified in the replication sample (x-axis). Values represent spatial correlation between average regional tau for each subtype. Values along the diagonal indicates similarity between the same subtype across both cohorts.

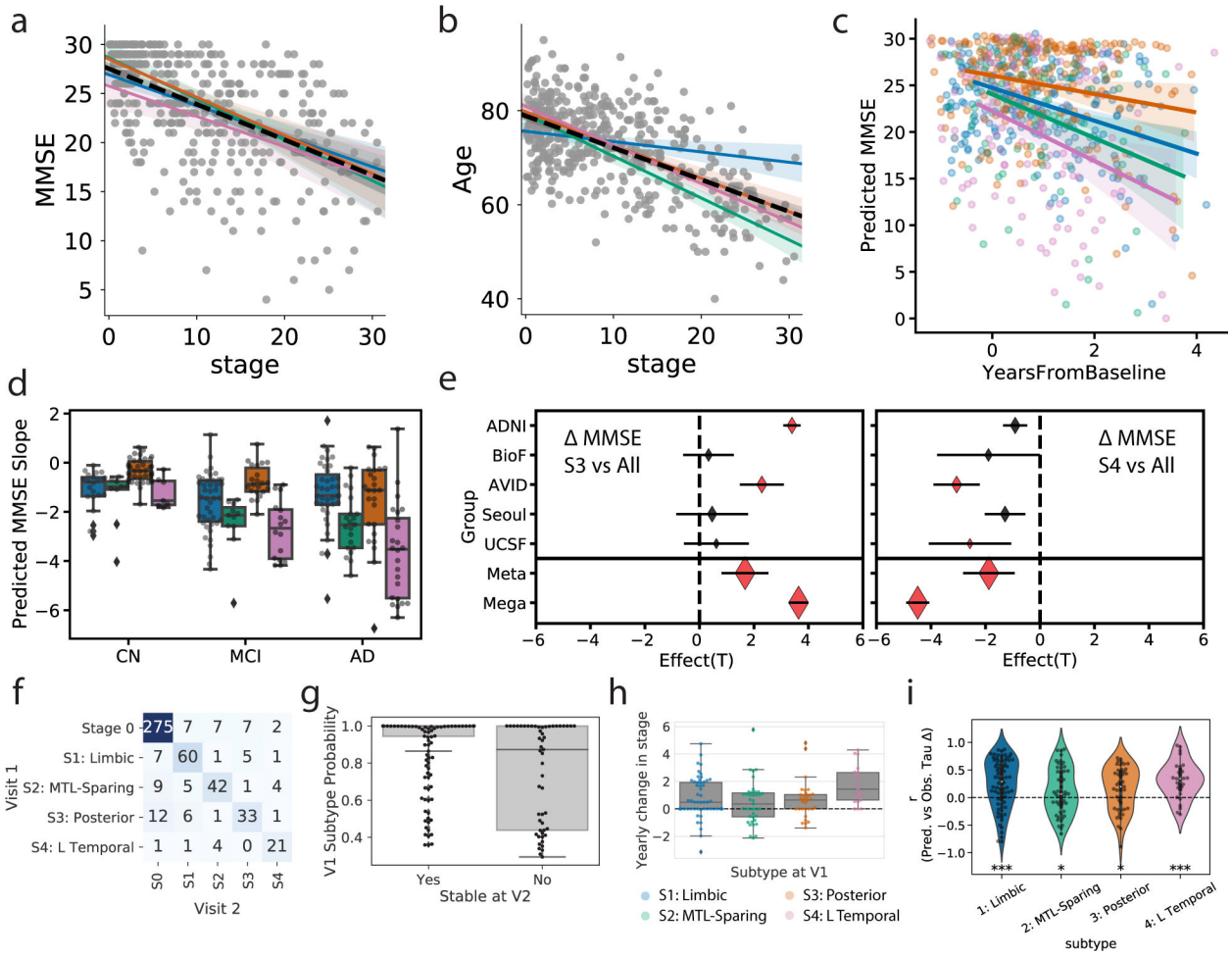

Figure 3.

Progression of AD subtypes. Increasing SuStaIn stage is associated with lower age a) and worse cognition b) across all subtypes. c) Rate of longitudinal decline in MMSE for each subtype. The x-axis was jittered for visualization purposes only. The y-axis shows MMSE across all observations as predicted by linear mixed models adjusted for covariates. d) Boxplots showing the distribution of predicted MMSE slopes for each subtype, stratified by clinical diagnosis (stats in Supplementary Table S2). e) Cross-cohort meta-analysis for the effects of S4: L Temporal declining faster (left) and S3: Posterior declining slower (right) than other subtypes, respectively. Diamonds represent effect sizes, while diamond size reflects relative sample size. Red diamonds indicate significant effects. Error bars = SEM. f) Confusion matrix showing longitudinal stability of subtypes. Each row shows the number of subjects from a given subtype at Visit 1 that were classified as each subtype at Visit 2. The diagonal represents the number of subjects that were classified as the same subtype at Visit 1 and Visit 2. g) Individuals with a higher probability of being classified into their subtype at baseline were more likely to show a stable subtype over time (two-sided t[156,53]=5.26, p=3.6e-07). h) Annual change in SuStaIn stage for each subtype, in individuals with stable subtypes over time (stats in Supplementary Note 3). i) SuStaIn was used to predict longitudinal change in regional tau accumulation. Each dot represents a

subject, and the y-axis represents the spatial correlation between the true regional tau change and the predicted regional tau change. Average predictions were significantly greater than chance based on a two-tided, one-sample t-test against 0 (S1: t[78]=5.00,p=3.5e-06; S2: t[52]=2.16,p=0.035; S3: t[45]=3.05,p=0.0039; S4: t[29]=4.93,p=3.1e-05). *p(unc.)<0.05, *** p(unc.)<0.001. Error bars in a-c represent 95% CI of model fit across 1000 bootstrap samples. For boxplots in d, g-i, center line=median, box=inner quartiles, whiskers=extent of data distribution except *=outliers

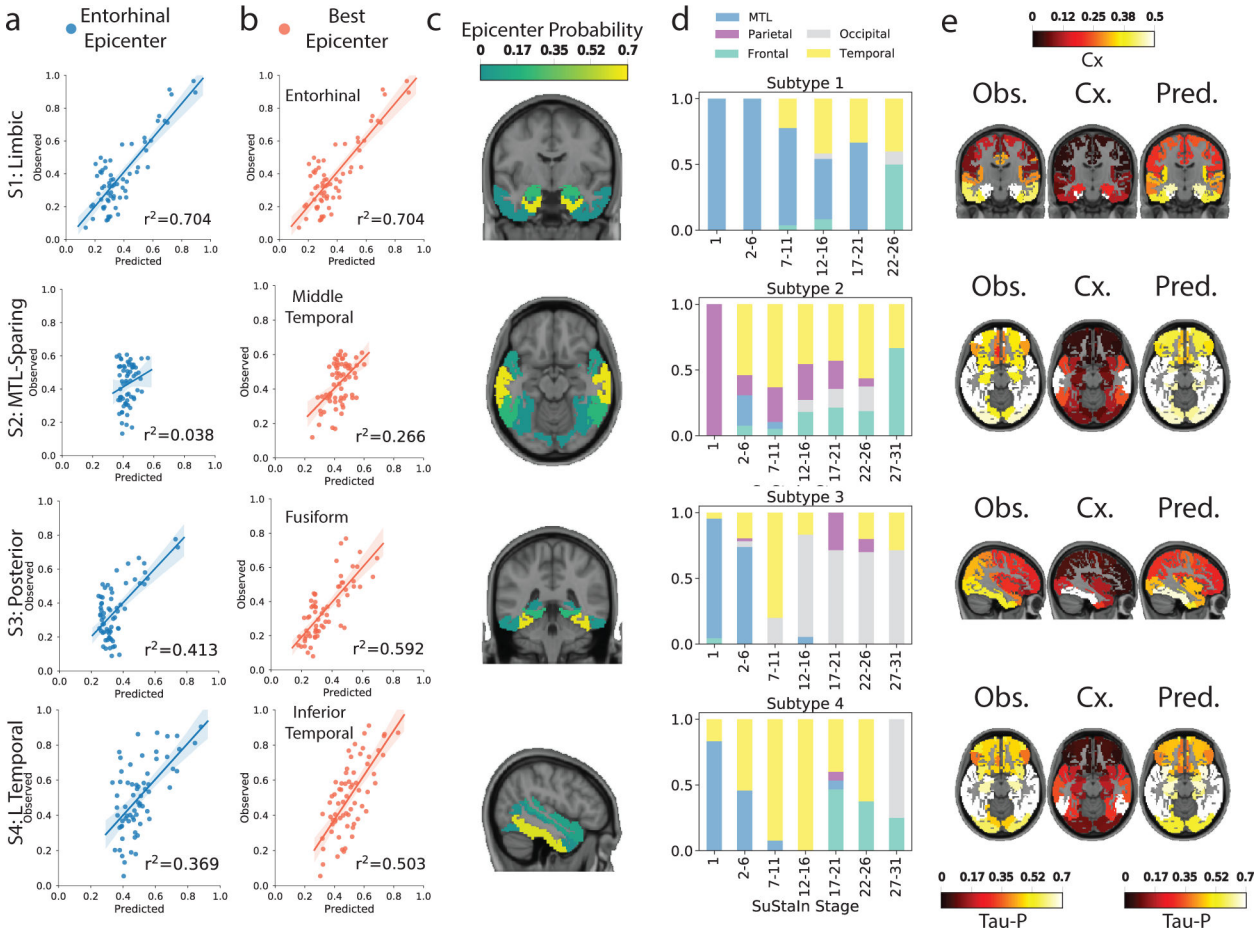

Figure 4.

Application of epidemic spreading model to determine subtype-specific corticolimbic circuit vulnerability. An epidemic spreading model was fit separately for each subtype; once using an entorhinal cortex epicenter (a, blue), and once with a subtype-specific best-fitting epicenter (b, red). For each plot, each dot represents a region. The x-axis represents the mean simulated tau-positive probabilities across the population, while the y-axis represents the mean observed tau-positive probability. Each row represents a subtype. Error bars in a-c represent 95% CI of model fit across 1000 bootstrap samples. c) For each subtype, the probability that each region is the best fitting epicenter for that subtype, based on bootstrap resampling. d) For each subtype, the proportion of individuals at various stages that had best-fitting epicenters within each of five major brain divisions: medial temporal lobe (MTL, blue), temporal lobe (yellow), parietal lobe (purple), occipital lobe (gray) and frontal lobe (turquoise). e) For each subype, spatial representation of ESM results from panel B using best-fitting epicenter. From left to right, observed regional tau-PET probabilities (tau-P), regional connectivity to best-fitting epicenter (Cx), tau-PET probabilities predicted by the ESM. These images show the degree to which constrained diffusion of signal through a connectome (Pred.), starting in a given epicenter and its associated fiber network (Cx.), recapitulates the tau patterns of each subtype (Obs.).

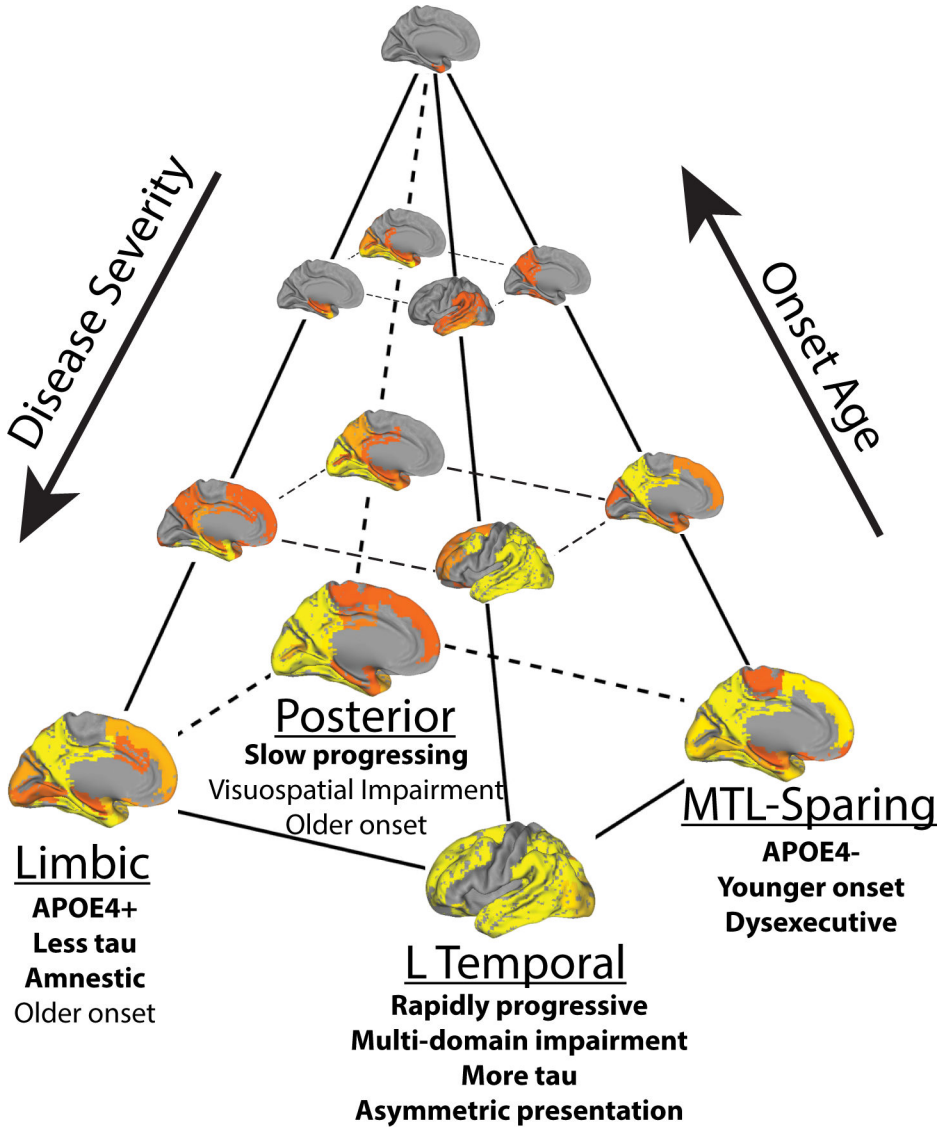

Figure 5.

A theoretical model summarizing variation in the spread of tau pathology in AD. Tau pathology varies along an axis of severity (vertical in the diagram), which is inversely associated with onset age. In addition, tau varies along a spatiotempral dimension (horizontal plane in the diagram), such that an individual can be described by their fit along one of at least four trajectories. Text indicates clinical characteristics of each subtypes. Emboldened text reflects robust differences between subtypes, while normal text reflects less-robust characteristics that differentiate subtypes from tau-negative individuals

Table 1

Comparison of means of different variables between subtypes in the discovery sample, after correction for age (except in the case of age), sex (except in the case of sex), education (except in the case of education), cohort, clinical diagnosis (i.e. CN, MCI, AD), and SuStaIn stage (except comparisons with S0). Standard deviations are given in parentheses where relevant. All p-values were corrected for multiple comparisons.

	S0: No Tau	S1: Limbic	S2: MTL-Sparing	S3: Posterior	S4: L Temporal
n	687	137	73	131	80
Age	71.52 (8.1)	75.28 (7.7)$^{\#}$	71.34 (8.3)*	75.06 (7.3)$^{\#}$	73.41 (6.9)
Prop. Female	0.49	0.70$^{\#}$	0.60‡	0.64$^{\#}$	0.56
Education	15.17 (2.9)	14.42 (3.9)	14.29 (4.0)	14.6 (3.0)	14.82 (2.9)
Prop. APOE4 Carrier	0.26	0.75$^{\#*}$	0.47*	0.63$^{\#}$	0.59$^{\#}$
Cortical Tau SUVR	1.04 (0.1)	1.41 (0.1)$^{\#*}$	1.44 (0.1)$^{\#}$	1.44 (0.1)$^{\#}$	1.47 (0.1)$^{\#*}$
Laterality	0.0 (0.2)	−0.28 (1.3)$^{*\#R}$	−0.13 (1.6)^{‡*R}	0.04 (1.5)	1.95 (1.2)$^{\#*L}$
MMSE	28.9 (1.5)	24.33 (3.0)$^{\#}$	24.32 (4.2)$^{\#}$	24.19 (3.0)$^{\#}$	23.33 (5.0)$^{\#}$
Global Cognition	0.36 (0.5)	−0.03 (0.8)*	−0.29 (0.8)$^{\#}$	−0.23 (0.8)$^{\#}$	−0.39 (0.9)$^{\#\dagger}$
Abs. Memory	0.48 (0.7)	−0.62 (0.7)$^{\#\dagger}$	−0.36 (0.7)$^{\#}$	−0.55 (0.7)$^{\#}$	−0.3 (0.8)$^{\#\dagger}$
Abs. Language	0.22 (0.7)	−0.11 (0.8)	0.01 (0.9)	−0.18 (0.8)	−0.64 (1.1)$^{\#*}$
Abs. Executive	0.19 (0.6)	0.02 (0.9)	−0.33 (0.9)$^{\#}$	0.03 (0.8)	−0.17 (1.0)‡
Abs. Visuospatial	0.19 (0.6)	0.08 (1.0)	−0.25 (1.2)$^{\#}$	−0.23 (1.2)$^{\#}$	−0.09 (1.0)
Rel. Memory	0.26 (0.8)	−0.61 (1.0)$^{\#*}$	−0.14 (1.0)	−0.37 (1.0)$^{\#}$	−0.06 (1.1)*
Rel. Language	−0.02 (0.8)	0.05 (1.0)	0.31 (1.2)$^{\#}$	0.06 (1.0)	−0.51 (1.3)$^{\#*}$
Rel. Executive	−0.14 (0.8)	0.25 (1.0)‡	−0.22 (1.0)‡*	0.38 (1.1)$^{\#}$	0.22 (1.2)
Rel. Visuospatial	−0.1 (0.7)	0.31 (1.1)‡	0.03 (1.3)	0.0 (1.3)	0.27 (1.3)

MMSE = Mini-Mental State Examination; Abs. = Absolute; Rel. = Relative; Prop. = Proportion

*= Adj. p$<$0.05 (vs all other subtypes, not including S0)

†= Adj. p$<$0.1 (vs all other subtypes, not including S0)

$^{\#}$= Adj. p$<$0.05 (vs S0)

‡= Adj. p$<$0.1 (vs S0).

^{R}= Significant right-sided laterality in this subtype compared to others

^{L}= Significant left-sides laterality in this subtype compared to other subtypes.